J. Fluid Mech. (2010), *vol.* 647, *pp.* 421–452.
doi:10.1017/S0022112010000066

Turbulent drag reduction and multistage transitions in viscoelastic minimal flow units

LI XI AND MICHAEL D. GRAHAM†

Department of Chemical and Biological Engineering, University of Wisconsin-Madison, Madison, WI 53706-1691, USA

(Received 8 June 2009; revised 22 December 2009; accepted 28 December 2009)

The observation that addition of a minute amount of flexible polymers to fluid reduces turbulent friction drag is well known. However, many aspects of this drag reduction phenomenon are not well understood; in particular, the origin of the maximum drag reduction (MDR) asymptote, a universal upper limit on drag reduction by polymers, remains an open question. This study focuses on the drag reduction phenomenon in the plane Poiseuille geometry in a parameter regime close to the laminar–turbulent transition. By minimizing the size of the periodic simulation box to the lower limit for which turbulence persists, the essential self-sustaining turbulent motions are isolated. In these 'minimal flow unit' (MFU) solutions, a series of qualitatively different stages consistent with previous experiments is observed, including an MDR stage where the mean flow rate is found to be invariant with respect to changing polymer-related parameters. Before the MDR stage, an additional transition exists between a relatively low degree (LDR) and a high degree (HDR) of drag reduction. This transition occurs at about 13 %–15 % of drag reduction and is characterized by a sudden increase in the minimal box size, as well as many qualitative changes in flow statistics. The observation of LDR–HDR transition at less than 15 % drag reduction shows for the first time that it is a qualitative transition instead of a quantitative effect of the amount of drag reduction. Spatio-temporal flow structures change substantially upon this transition, suggesting that two distinct types of self-sustaining turbulent dynamics are observed. In LDR, as in Newtonian turbulence, the self-sustaining process involves one low-speed streak and its surrounding streamwise vortices; after the LDR–HDR transition, multiple streaks are present in the self-sustaining structure and complex intermittent behaviour of the streaks is observed. This multistage scenario of LDR–HDR–MDR recovers all key transitions commonly observed and studied at much higher Reynolds numbers.

1. Introduction

It has been experimentally observed that by introducing a minute amount of flexible polymers (at concentrations of $O(10–100)$ ppm by weight or even lower) into a turbulent flow, the turbulent friction drag can be substantially reduced (Virk 1975; Graham 2004; White & Mungal 2008), resulting in a higher flow rate for a given pressure drop. The reduction in friction factor can be as high as 80 % in turbulent flows in straight pipe or channel geometries. Since its initial discovery in the

† Email address for correspondence: graham@engr.wisc.edu

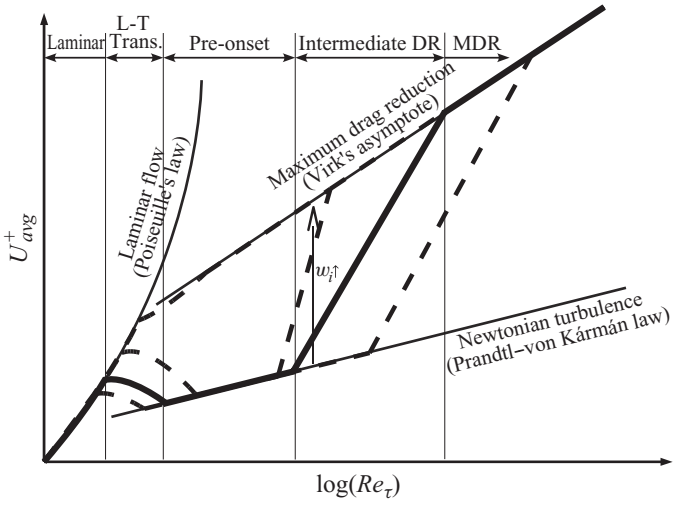

FIGURE 1. Schematic Prandtl–von Kármán plot. Thin vertical lines mark transitions on the typical experimental path shown as a thick solid line.

1940s (Toms 1948, 1977), the phenomenon of polymer drag reduction has been an active area of study due to its practical and theoretical significance. It can obviously be utilized to improve energy efficiency in various fluid transportation applications. Moreover, unraveling the physical mechanism of the phenomenon in terms of the complex interactions between turbulence and polymer molecules would not only expand our knowledge of polymer dynamics in fluid flows but also provide additional insight into the nature of turbulence itself.

Bulk flow data obtained from drag reduction experiments are often plotted in Prandtl–von Kármán coordinates, i.e. as a plot of average velocity $U^+_{avg} \equiv U_{avg}/u_\tau$ versus friction Reynolds number $Re_\tau \equiv \rho u_\tau l/\eta$. (Here, ρ is the fluid density, η is the total viscosity and l is a characteristic length scale of the flow geometry; the friction velocity $u_\tau \equiv \sqrt{\tau_w/\rho}$ is a characteristic velocity scale for near-wall turbulence, where τ_w is the mean wall shear stress; the superscript '+' denotes quantities non-dimensionalized with inner scales, i.e. velocities scaled by u_τ and lengths scaled by $\eta/\rho u_\tau$. We also define $Re \equiv \rho U l/\eta$ as the Reynolds number using the characteristic bulk flow velocity U as the velocity scale and $Wi \equiv \lambda\dot{\gamma}$ as the Weissenberg number, which is the product of polymer relaxation time λ and a characteristic shear rate $\dot{\gamma}$. Note that $\dot{\gamma} \propto U/l$.) A schematic Prandtl–von Kármán plot for Newtonian and polymeric flow is shown in figure 1. Along a typical experimental path, where the polymer solution system and the pipe/channel size are fixed, Re and Wi vary simultaneously while their ratio, defined as the elasticity number $El \equiv Wi/Re$, remains constant. One such path is drawn as a thick solid line in figure 1. With increasing Re_τ, the flow system undergoes a series of transitions among several qualitatively different stages, including laminar flow, laminar–turbulence transition, turbulence before the onset of drag reduction (pre-onset), intermediate drag reduction and the maximum drag reduction (MDR) asymptote, a term coined by Virk (1975). The boundaries of each stage (i.e. the transition points) are marked with thin vertical lines for the experimental path denoted by the thick solid line. The last stage (MDR) is so named because it is invariant with changing polymer species, molecular weight, concentration and geometric-confinement length scale (pipe diameter or channel height) (Virk 1975;

Graham 2004; White & Mungal 2008). Experimental paths of different polymer solution systems and/or pipe/channel sizes are sketched by dashed lines. Although changing the polymer solution system and/or the confinement length scale, e.g. via changes in *El*, would affect the slope in the intermediate DR stage as well as the points of transition, all experimental paths collapse into a single straight line after they reach the MDR stage. This line, commonly referred to as the Virk MDR asymptote, sets the universal upper limit of drag reduction when polymer is used as the drag-reducing agent. Note that once this asymptote is reached, the friction drag is solely dependent on Re_τ. This universality of the MDR stage, first recognized by Virk, is widely regarded as the most intriguing problem in polymer drag reduction.

The study of polymer-induced drag reduction thus can be divided into several important questions: (i) what is the mechanism by which polymers alter turbulence and reduce drag; (ii) what are the qualitative changes underlying these multistage transitions; and in particular (iii) why is there a universal upper limit on drag reduction (MDR) and what is the nature of turbulence in that regime?

None of these questions has been completely answered to date; however, advances in computer simulations of viscoelastic turbulent flows in the past decade have substantially advanced the understanding of drag reduction. Beris and coworkers pioneered the direct numerical simulation (DNS) of viscoelastic turbulent flows (Sureshkumar & Beris 1997; Dimitropoulos, Sureshkumar & Beris 1998) using the FENE-P (Bird *et al.* 1987) constitutive equation. Most major experimental observations in the intermediate drag reduction regime (after onset and before MDR), including the onset of drag reduction, thickened buffer layer, wider streak spacing and changes in the velocity fluctuations and Reynolds shear stress profiles, were qualitatively reproduced. Since then DNS has been adopted as a powerful tool to access the details of velocity and polymer stress fields and thus to infer the mechanism(s) by which polymers reduce drag. By inspecting the instantaneous snapshots of velocity fluctuations and polymer force fields, as well as the correlation between the two, De Angelis, Casciola & Piva (2002) claimed that polymer suppresses turbulence by counteracting the velocity fluctuations. (This mechanism is also predicted by other means (Stone, Waleffe & Graham 2002; Stone *et al.* 2004; Li & Graham 2007), as we discuss below.) Similar results on the velocity–polymer force correlations were reported by Dubief *et al.* (2004, 2005), who showed that polymer forces are anti-correlated with velocity fluctuations in the transverse directions, while in the streamwise direction these two quantities are positively correlated in the viscous sublayer and anti-correlated for the rest of the channel. On the basis of this observation, they suggested that polymer molecules suppress the vortical motions and meanwhile are stretched by these near-wall vortices; when they are convected towards the wall to the high-speed streaks during the 'sweeping' events, they release the energy back to the flow and thereby aid in the sustenance of turbulence.

Another common practice to interpret DNS data is to examine the transport equations of kinetic energy and Reynolds stresses and describe the effects of polymer in terms of the changes it causes to different contributions to the energy budgets. Min *et al.* (2003*b*) proposed that the kinetic energy of the turbulent flow is transferred to elastic energy via stretching of the polymer molecules very close to the wall; these stretched molecules are lifted upward to the buffer and log-law layers to release energy back to the flow. Ptasinski *et al.* (2003) evaluated the budget of each component of the turbulent kinetic energy and found that polymer suppresses pressure fluctuations and thus impedes energy transfer among different components via the pressure rate of strain term in the Reynolds stress budgets.

The studies mentioned above primarily rely on statistical representations of the three-dimensional fields, quantities averaged in time as well as in the two periodic dimensions. Although this approach addresses many quantities of interest, it does not provide structural information about the turbulent motions. On the other hand, in the near-wall region, where most drag reduction effects caused by polymer originate, turbulent flows are known to be dominated by coherent structures (Robinson 1991) – indeed these near-wall structures 'export' turbulent kinetic energy to the rest of the flow (Jiménez & Pinelli 1999). Further understanding of the interplay between turbulent structures and polymer dynamics requires the capability of isolating the coherent structures from the complex turbulent background.

Information about these coherent structures can be extracted from DNS solutions *a posteriori*. For example, the Karhunen–Loéve analysis (or proper orthogonal decomposition) (Holmes, Lumley & Berkooz 1996) has been applied to viscoelastic turbulent flows for this purpose (De Angelis *et al.* 2003; Housiadas, Beris & Handler 2005). Given a set of statistically independent snapshots from the time-dependent turbulent flow, this method constructs a series of mutually orthogonal modes, or eigenfunctions, which form an optimal decomposition of the original flow in the sense that the leading modes always contain the largest amount of turbulent kinetic energy. These studies showed that viscoelasticity modifies the turbulent flow by increasing the amount of energy carried by these leading modes. However, further study is still needed to connect this finding with the dynamic process of polymer–turbulence interactions. More recently, conditional averaging has been used to sample the predominant structures around certain local events that contribute substantially to the turbulent friction drag (Kim *et al.* 2007). These results confirmed that polymer inhibits vortical motions, both streamwise vortices in the buffer layer and hairpin vortices farther away from the wall, by applying forces that counter them. This is consistent with many other studies (De Angelis *et al.* 2002; Stone *et al.* 2002, 2004; Dubief *et al.* 2005; Li & Graham 2007). Using these sampled structures as the initial conditions for time integration, evolution of the hairpin vortices was simulated (Kim *et al.* 2008), and it was found that viscoelasticity not only suppresses the primary vortices but also prevents secondary vortices from being created.

In the past decade, the discovery of three-dimensional fully nonlinear relative steady-state solutions, or travelling wave (TW) solutions, to the Navier–Stokes equation has made the *a priori* study of the coherent structures a reality. These solutions are steady states of the Navier–Stokes equation typically in a reference frame moving at a constant speed, and they are found in all canonical wall-bounded geometries (plane Couette, plane Poiseuille and pipe) (Waleffe 1998, 2001, 2003; Faisst & Eckhardt 2003; Pringle & Kerswell 2007; Viswanath 2007). These TWs usually have a structure composed of low-speed streaks straddled by streamwise vortices, which closely (in both structure and length scales) resemble the recurrent coherent structures in near-wall turbulence. In particular, the optimal spanwise box size of 105.51 wall units reported for the TW solution found by Waleffe in the plane Poiseuille geometry (Waleffe 2003) is remarkably close to the experimentally observed near-wall streak spacing of about 100 wall units (Smith & Metzler 1983). Furthermore, the Reynolds number (based on laminar centreline velocity) at which these TWs first appear, $Re = 977$ is very close to the experimentally observed value of 1×10^3 (Carlson, Widnall & Peeters 1982). Transient structures that look very similar to these solutions have been experimentally observed (Hof *et al.* 2004). In the context of drag reduction, past work has examined one family of these TW solutions, the 'exact coherent states' (ECS; Waleffe 1998, 2001,

2003) of viscoelastic turbulent flows in both plane Couette (Stone *et al.* 2002, 2004; Stone & Graham 2003) and plane Poiseuille geometries (Li, Stone & Graham 2005; Li, Xi & Graham 2006*b*; Li & Graham 2007). Not only do the viscoelastic ECS solutions show drag reduction compared with their Newtonian counterparts, they also capture many characteristics of drag-reduced turbulence, including reduced vortical strength and changes in turbulence statistics. Consistent with DNS results (De Angelis *et al.* 2002; Dubief *et al.* 2005; Kim *et al.* 2007), the polymer influences the flow structures and causes drag reduction in ECS by counteracting velocity fluctuations and vortical motions (Stone *et al.* 2002, 2004; Li & Graham 2007). Viscoelasticity also changes the minimal *Re* at which ECS exist; under fixed *Re* and with high enough *Wi*, these solutions are totally suppressed by the polymer (Stone *et al.* 2004; Li *et al.* 2006*b*; Li & Graham 2007). Based on these studies, a simple framework containing different stages of the ECS solutions in the parameter space, which includes the laminar–turbulence transition, the onset of drag reduction and the annihilation of ECS, was proposed (Li *et al.* 2006*b*; Li & Graham 2007). With the hypothesis that the annihilation of ECS is linked with MDR, this framework covered most key transitions in viscoelastic turbulent flows.

Although viscoelastic ECS solutions do provide new insight into the problem of drag reduction, they are only fixed points (i.e. steady states) in state space. Turbulence, on the other hand, is a complex time-dependent trajectory, so further investigation into the coherent turbulent motions requires the study of transient solutions. The DNS studies mentioned earlier belong to this category, but in most of them, periodic simulation boxes much larger than the characteristic length scales of the coherent structures are used. Transient solutions obtained from that approach typically involve a large number of coherent structures convoluted with one another and include the long-range spatial correlations between them, which makes the identification and analysis of individual coherent structures difficult. The most straightforward way to isolate the transient solution corresponding to an individual coherent structure is the 'minimal flow unit' (MFU) approach: by limiting the simulation box to the smallest size that still sustains the turbulent motion, this approach includes in the simulation only the very essential elements of the self-sustaining process of turbulence. This approach was proposed by Jiménez & Moin (1991) in the context of Newtonian turbulent flows. The minimal spanwise box size in inner scales they found, $L_z^+ \approx 100$, is in very good agreement with the experimental measurement of the streak spacing in the viscous sublayer (Smith & Metzler 1983), and this value is insensitive to the change of *Re*. The minimal streamwise box size they reported is dependent on *Re* and falls in the range of $250 \lesssim L_x^+ \lesssim 350$, which is also consistent with experimental measurements of the streamwise structure spacings (Sankaran, Sokolov & Antonia 1988). By comparing transient trajectories of MFU simulations with various TW solutions in certain two-dimensional projections of the state space, Jiménez *et al.* (2005) described the dynamical process of MFU in plane Poiseuille and Couette geometries as a combination of relatively long-time stays in the vicinity of the TWs ('equilibrium') and intermittent excursions away from these states ('bursting'). A different result is obtained in pipe flows: Kerswell & Tutty (2007) proposed several correlation functions as quantitative measurements of the distance between transient solutions and TWs, and observed that the transient turbulent trajectories only visit the TWs about 10 % of the time and more complex objects in the state space, such as periodic orbits, are necessary for a good approximation of the time-dependent solutions. In the plane Couette geometry and using coordinates constructed with upper branch ECS solutions and symmetry arguments, Gibson, Halcrow & Cvitanotić

(2008) visualized the trajectories of MFU solutions together with the TW states and their unstable manifolds in a geometrical view of the state space, with which the connection between transient solutions and the dynamical structure formed by TWs can been clearly seen.

All these studies on MFU are focused on Newtonian turbulent flows. Despite the simplicity and power behind the MFU idea, this approach has not been directly applied in the study of viscoelastic turbulence and drag reduction, partially due to the additional degrees of freedom in the parameter space when polymer is introduced. While Newtonian flows can be characterized by a single parameter *Re*, this is no longer true in polymer solutions where polymer species, molecular weight and concentration can also affect the flow dynamics and hence minimal box sizes. To search for the minimal box size therefore becomes a highly computationally demanding task when variations in all parameters are taken account of. Since the term MFU is often used by other authors (e.g. Min *et al.* 2003*b*; Ptasinski *et al.* 2003; Dubief *et al.* 2005) to describe DNS in relatively small, but not necessarily minimal, boxes, we emphasize here that in this paper, the term 'minimal flow unit' will refer exclusively to a flow determined via a size minimization process. That is, for each parameter setting, different box sizes are tested in order to determine a minimal size at which turbulence persists. As we discuss in § 3, in the present study the minimization process is only taken in the spanwise direction, while the streamwise box size is fixed at the value of the Newtonian MFU. The goal of the current work is to find the MFU of viscoelastic turbulence under a variety of parameters and observe the transitions among different stages in terms of drag reduction behaviours.

A classical picture of the stages of viscoelastic turbulence includes pre-onset turbulence, intermediate DR (after onset and before MDR) and MDR (figure 1). Compared with the extensive studies of the intermediate DR regime summarized earlier, the research on MDR is very limited. Though there is a certain degree of understanding of the phenomenon of how polymer additives reduce turbulent drag, the origin of the universal upper limit in the MDR stage remains very poorly understood.

Early theory of Virk (1975) assumed that drag reduction only occurs in the buffer layer; as viscoelasticity increases, the thickness of this layer increases, and MDR is reached when the buffer layer dominates the whole flow geometry. This view is similar to the conclusion drawn from the elastic theory of Sreenivasan & White (2000), that at MDR the length scale of turbulence structure affected by polymer is comparable with that of the flow geometry, and indeed this view is consistent with the results presented below. Based on these views, phenomenological models have been developed to predict mean velocity profiles, in which quantitative agreement with the Virk MDR profile was reported (Benzi *et al.* 2006; Procaccia, L'vov & Benzi 2008). These models have achieved various levels of success in capturing many experimental results; however, discrepancies are still found with some other observations, as discussed by White & Mungal (2008). In addition, all these theoretical studies are based on average (in both space and time) quantities; the lack of information in these models about turbulent coherent structures and their spatio-temporal behaviour limits their ability to contribute to a physical picture of the dynamics underlying experimental observations.

Among the few DNS studies on MDR, most efforts are dedicated to reproducing the Virk mean velocity profile of MDR (Ptasinski *et al.* 2003; Dubief *et al.* 2005; Li, Sureshkumar & Khomami 2006*a*): i.e. they look for parameter settings under which the mean velocity profile of DNS is the same as or close to that of experimentally

observed MDR at Re far from transition, which according to Virk (1975) is universal in inner scales for a wide range of Re. The only exception to our knowledge is the work of Min, Choi & Yoo (2003*a*), where the convergence of $DR\,\%$ with increasing Wi is used to identify MDR. (The percentage of drag reduction, $DR\,\% \equiv (C_{f,s} - C_f)/C_{f,s} \times 100\,\%$, where $C_f \equiv 2\tau_w/(\rho U_{avg}^2)$ is the friction factor of the viscoelastic fluid flow, and $C_{f,s}$ is the friction factor of the flow of pure solvent.) In that study, $DR\,\%$ of several Wi is calculated with other parameters held fixed, and the last two points on the high Wi end show almost the same $DR\,\%$. As mentioned earlier, MDR is a stage where the friction factor is only dependent on Re, and is unaffected by variations in Wi and other polymer-related properties; therefore the problem of MDR is the mechanism by which the same friction factor is preserved at fixed Re with changing polymer parameters. This mechanism cannot be studied without simulation data at MDR for a range of different parameter settings. Furthermore, whether one should expect the same mean velocity profile in DNS studies as that of Virk is uncertain: first, most experiments on MDR are conducted at relatively high Re, and the lack of experimental measurements in the regime close to the laminar–turbulence transition makes it hard to conclude whether the Virk profile is valid at Re comparable to those in many DNS studies; second, the widely used FENE-P constitutive equation is a highly simplified model for polymer molecules and how well it can quantitatively predict the mean velocity at MDR is still unknown. In the simulations of Min *et al.* (2003*a*), the limiting mean velocity profile at high Wi is clearly lower than the Virk MDR profile; Dubief *et al.* (2005) also reported that the Virk MDR profile is only obtained in a relatively small simulation box, and is not found in large-box simulations; a small box is also used in the study of Ptasinski *et al.* (2003). The only DNS study that predicts mean velocity profiles comparable to Virk's in large simulation boxes is that of Li *et al.* (2006*a*). However, they did not report the universal convergence of the mean velocity. In the present work, we identify MDR by using the criterion that the friction factor converges with increasing Wi at fixed Re.

In recent years, an additional distinction was noticed within the intermediate DR regime between a low degree of drag reduction (LDR) and a high degree of drag reduction (HDR). This difference was investigated by Warholic, Massah & Hanratty (1999) in their plane Poiseuille flow experiments, where differences between LDR and HDR appear in several statistical quantities, including: (i) mean velocity profile: LDR has the same log-law slope as Newtonian turbulent flows while HDR shows larger slope of the log-law; (ii) streamwise velocity fluctuation profile: at LDR the magnitude of fluctuations (in inner scales) increases with $DR\,\%$ and the location of the peak shifts away from the wall, while at HDR fluctuations are greatly suppressed compared with Newtonian turbulent flows; (iii) wall-normal velocity fluctuation profile: fluctuations are suppressed in both cases but at LDR there is still a recognizable maximum in the profile while at HDR the maximum is not observable; (iv) Reynolds shear stress profile: at LDR the Reynolds shear stress decreases with DR but the profile retains the same slope as that of Newtonian turbulent flows at large distance away from the wall, while at HDR the Reynolds shear stress is almost zero across the channel and the slope farther away from the wall also changes significantly. Some of these differences have also been noted by several other groups through both experiments (Ptasinski *et al.* 2003) and simulations (Min *et al.* 2003*a*; Ptasinski *et al.* 2003; Li *et al.* 2006*a*). Most authors tend to treat these differences as quantitative effects of the percentage of drag reduction $DR\,\%$, and $DR\,\% \approx 30\,\%$–$40\,\%$ is commonly adopted as the separating point between LDR and HDR.

As stated earlier, in this work we look for MFU solutions, i.e. time-dependent solutions containing the minimal self-sustaining structures, of viscoelastic turbulent flows. A wide range of parameter space is sampled in order to provide a complete picture of the different stages in terms of drag reduction behaviours. Note that although experimental measurements are typically made following paths with constant *El*, along which *Re* and *Wi* are varying simultaneously (cf. figure 1), in this study (as in many others, for example Sureshkumar & Beris 1997, Min *et al.* 2003*a* and Li *et al.* 2006*a*), we focus on the behaviour as a function of *Wi* while holding *Re* fixed. As shown by the vertical arrow in figure 1, one can still visit all different stages of transition, on different experimental paths, by varying *Wi* under fixed *Re*; the advantage of doing so is that the MDR stage can be easily identified as a plateau on the bulk flow rate versus *Wi* curve. Our results show that all the stages of transition previously reported from both experiments and full-scale DNS studies, including pre-onset turbulence, LDR, HDR and MDR, are observed in these solutions in MFUs. In particular, we indicate the changes in spatio-temporal structure that accompany the LDR–HDR transition and identify a regime in which $DR\,\%$ converges with increasing *Wi*, i.e. the MDR stage. We have varied all the parameters (except *Re*) in the system and there is no statistically significant difference in the bulk flow rate with changing parameters once the MDR stage is reached. This is, to our knowledge, the first report of MDR in numerical simulations that matches its qualitative experimental hallmark: the bulk flow rate is only a function of *Re*. In addition, all simulation results reported in this paper are obtained at a *Re* lower than any previously published DNS study, close to the laminar–turbulence transition. The fact that all these key stages of viscoelastic turbulence (especially MDR) can be studied in the parameter regime close to the laminar–turbulence transition, as predicted in earlier work (Li *et al.* 2006*b*; Li & Graham 2007), is important not only from the computational point of view (computational cost grows rapidly with increasing *Re*) but also in terms of the understanding of the turbulent structures (at *Re* this low, the near-wall coherent structures dominate the whole flow geometry and are easier to observe). We also need to mention that the highest $DR\,\%$ reached in our simulations only in the range of 20 %–30 %, which is clearly below the separating point between LDR and HDR identified in other studies. The fact that the LDR–HDR transition exists at such low $DR\,\%$ indicates that it is a transition between two qualitatively different stages during the drag reduction process instead of a quantitative difference associated with the amount of drag reduction.

This paper is organized as follows. Section 2 summarizes the mathematical formulation and numerical method. In § 3, we discuss in detail the process of finding minimal flow units. Discussion of results (§ 4) is divided into several parts: we start with an overview of the multistage-transition scenario in MFU solutions for a variety of polymer-related parameters (§ 4.1); then we present flow and polymer conformation statistics (§§ 4.2 and 4.3) at different stages for the sake of comparison with existing publications; finally, in § 4.4 we study the spatio-temporal structure of the self-sustaining dynamics, which provides insight into the changes in turbulence dynamics accompanying the multistage transitions. The paper is concluded in § 5.

2. Formulation

2.1. *Flow geometry and governing equations*

We consider plane Poiseuille flow driven by a constant mean pressure gradient. The x, y and z coordinates are aligned with the streamwise, wall-normal and spanwise

directions, respectively. The no-slip boundary condition is applied at the walls and periodic boundary conditions are applied in the x and z directions; the periods in these directions are denoted by L_x and L_z. All lengths in the geometry are non-dimensionalized with the half-channel height l of the channel and the velocity scale is the Newtonian laminar centreline velocity U at the given pressure drop. Time t is scaled with l/U and pressure p with ρU^2. The conservation equations of momentum and mass give

$$\frac{\partial \boldsymbol{v}}{\partial t} + \boldsymbol{v}\cdot\nabla\boldsymbol{v} = -\nabla p + \frac{\beta}{Re}\nabla^2\boldsymbol{v} + \frac{2(1-\beta)}{ReWi}\left(\nabla\cdot\boldsymbol{\tau}_p\right), \tag{2.1}$$

$$\nabla\cdot\boldsymbol{v} = 0. \tag{2.2}$$

Here, $Re \equiv \rho U l/(\eta_s + \eta_p)$ (ρ is the total density of the fluid, and $(\eta_s + \eta_p)$ is the total zero-shear rate viscosity; hereinafter, the subscript 's' represents 'solvent', i.e. the Newtonian fluid, and the subscript 'p' represents the polymer contribution) and $Wi \equiv 2\lambda U/l$, which is the product of the polymer relaxation time λ and the mean wall shear rate. Under this definition, the friction Reynolds number, defined as $Re_\tau \equiv \rho u_\tau l/(\eta_s + \eta_p)$, can be directly related to Re: i.e. $Re_\tau = \sqrt{2Re}$. The viscosity ratio $\beta \equiv \eta_s/(\eta_s + \eta_p)$ is the ratio of the solvent viscosity and the total viscosity. For dilute polymer solutions, $1-\beta$ is approximately proportional to the polymer concentration. The last term on the right-hand-side of (2.1) captures the polymer effects on the flow field, where the polymer stress tensor $\boldsymbol{\tau}_p$ is modelled by the FENE-P constitutive equation (Bird *et al.* 1987):

$$\frac{\boldsymbol{\alpha}}{1-\dfrac{\mathrm{tr}(\boldsymbol{\alpha})}{b}} + \frac{Wi}{2}\left(\frac{\partial\boldsymbol{\alpha}}{\partial t} + \boldsymbol{v}\cdot\nabla\boldsymbol{\alpha} - \boldsymbol{\alpha}\cdot\nabla\boldsymbol{v} - (\boldsymbol{\alpha}\cdot\nabla\boldsymbol{v})^{\mathrm{T}}\right) = \left(\frac{b}{b+2}\right)\boldsymbol{\delta}, \tag{2.3}$$

$$\boldsymbol{\tau}_p = \frac{b+5}{b}\left(\frac{\boldsymbol{\alpha}}{1-\dfrac{\mathrm{tr}(\boldsymbol{\alpha})}{b}} - \left(1-\frac{2}{b+2}\right)\boldsymbol{\delta}\right). \tag{2.4}$$

In (2.3) and (2.4), polymer molecules are modelled as FENE dumbbells: two beads connected by a finitely extensible nonlinear elastic (FENE) spring; the Peterlin closure approximation yields a closed expression for $\boldsymbol{\alpha}$. The variable $\boldsymbol{\alpha}$ is the non-dimensional polymer conformation tensor $\boldsymbol{\alpha} \equiv \langle \boldsymbol{Q}\boldsymbol{Q}\rangle$, where $\boldsymbol{Q}$ is the end-to-end vector of the dumbbells. The parameter b defines the maximum extensibility of the dumbbells; $\max(\mathrm{tr}(\boldsymbol{\alpha})) \leqslant b$.

In this study, we fix $Re = 3600$ ($Re_\tau = 84.85$) and span the parameter space at three different (β, b) pairs, (0.97, 5000), (0.99, 10 000) and (0.99, 5000), with a large range of Wi for each β and b. The importance of β and b becomes apparent in considering the extensibility parameter Ex, defined as the polymer contribution to the steady-state stress in uniaxial extensional flow, in the high Wi limit. For the FENE-P model, $Ex = 2b(1-\beta)/3\beta$. For a dilute solution ($1-\beta \ll 1$), significant effects of polymer on turbulence are only expected when $Ex \gg 1$. For the three sets of β and b given above, the values of Ex are 103.09, 67.34 and 33.67, respectively.

2.2. *Numerical procedures*

The coupled problem of (2.1)–(2.4) is integrated in time with a third-order semi-implicit time-stepping algorithm: linear terms are updated with the implicit third-order backward differentiation method and nonlinear terms are integrated with the explicit third-order Adams–Bashforth method (Peyret 2002). The continuity equation

(see (2.2)) is coupled with the momentum balance (see (2.1)) using the influence matrix method (Canuto *et al.* 1988). The alternating form is used to evaluate the inertia term in (2.2): we switch between the convection form $\boldsymbol{v}\cdot\nabla\boldsymbol{v}$ and the divergence form $\nabla\cdot(\boldsymbol{vv})$ upon each time step (Zang 1991).

The Fourier–Chebyshev–Fourier spatial discretization is applied in all variables and nonlinear terms are calculated with the collocation method. The grid spacing for the streamwise direction is $\delta_x^+ = 8.57$, and in the spanwise direction we adjust the number of Fourier modes according to the varying box width (as discussed in § 3) to keep the grid spacing roughly constant in the range of $5.0 \leqslant \delta_z^+ \leqslant 5.5$; in the wall-normal direction, 73 Chebyshev modes are used, which gives $\delta_{y,min}^+ = 0.081$ at the wall and $\delta_{y,max}^+ = 3.7$ at the channel centre at $Re = 3600$. The time step size is determined from the Courant–Friedrichs–Lewy condition (CFL) stability condition: for the simulations reported in this paper, since the spatial grid spacing is fixed, a constant time step $\delta t = 0.02$ is used.

An artificial stress diffusion term $1/(ScRe)\nabla^2\boldsymbol{\alpha}$ is added to the right-hand side of (2.3), a common practice to improve numerical stability in pseudo-spectral simulations of viscoelastic fluids (Sureshkumar & Beris 1997; Dimitropoulos *et al.* 1998; Housiadas & Beris 2003; Ptasinski *et al.* 2003; Housiadas *et al.* 2005; Li *et al.* 2006*a*; Kim *et al.* 2007). In this study, we use a fixed value of the Schmidt number, $Sc = 0.5$, which gives a constant artificial diffusivity of $1/(ScRe) = 5.56 \times 10^{-4}$. The magnitude of this artificial diffusivity is of the same order as that used by previous studies of other groups, typically $O(10^{-4})$; an additional diffusive term at this order of magnitude should not affect the numerical solutions significantly while it helps to the numerical stability greatly. With the introduction of this term, an additional boundary condition is needed for (2.3), for which we used the solution without the artificial diffusivity (the same is done in many other viscoelastic DNS studies, e.g. Sureshkumar & Beris 1997): i.e. we update the $\boldsymbol{\alpha}$ values at the walls without the artificial diffusivity term first; using these results as the boundary values, we solve (2.3) with the artificial diffusivity term added to update the $\boldsymbol{\alpha}$ field for the rest of the channel.

3. Methodology: minimal flow units

The dimensions of the simulation box (L_x^+, L_z^+) determine the longest wavelengths captured in the numerical solutions. As introduced in § 1, the MFU approach finds the transient solutions of (2.1)–(2.4) that correspond to the self-sustaining coherent structures by finding the smallest box in which turbulent motions are sustained. Note that this minimal box size is in general a function of all parameters in the system, i.e. Re, Wi, β and b. Accordingly, the minimization process has to be performed for each different parameter combination. In Newtonian MFUs, a roughly constant value $L_z^+ \approx 100$ is found for different magnitudes of Re whereas L_x^+ decreases with increasing Re (Jiménez & Moin 1991). Experimentally measured steak spacings in turbulent flows of polymer solutions are larger than the 100 wall units found for Newtonian turbulent flows, and also increase with increasing DR % (Oldaker & Tiederman 1977; White, Somandepalli & Mungal 2004). This observation is consistent with large-box DNS results, where the length scales of spanwise spatial correlation functions increase with increasing DR % (Sureshkumar & Beris 1997; De Angelis *et al.* 2003; Li *et al.* 2006*a*). Therefore, L_z^+ larger than that of the Newtonian MFUs is expected in our search for viscoelastic MFUs. Viscoelasticity increases the correlation length scales in the streamwise direction as well. In particular, Li *et al.* (2006*a*) reported that the streamwise correlation length is increased by more than an order of magnitude when DR % increases from 0 to 60 % or more. As a result, a significantly longer simulation

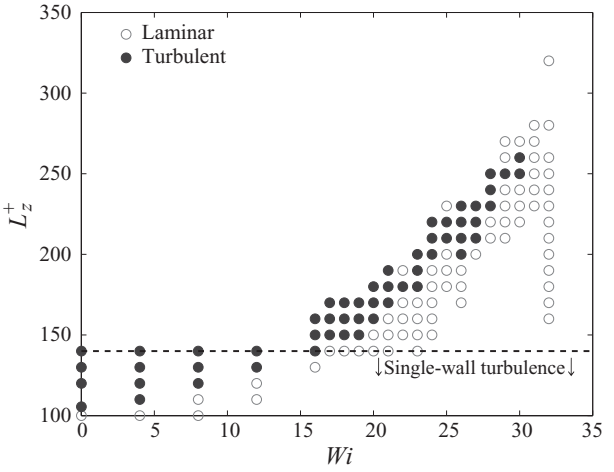

FIGURE 2. Summary of simulation results: 'Turbulent' indicates that at least one simulation run gives sustained turbulence within the given time interval ($\beta = 0.97$, $b = 5000$).

box is required to capture all these long-range correlations at high DR %. Consistent with these studies, the streamwise and spanwise optimal length scales of viscoelastic ECS solutions also increase with increasing Wi (Li & Graham 2007).

A rigorous search of MFUs should consider the parameter dependence of both L_x^+ and L_z^+, a task involving impractically large number of simulation runs. In this study, we fix $L_x^+ = 360$ and focus on the variation of L_z^+ only. Although both length scales depend on parameters, L_z^+ is arguably the quantity of more interest: the dominant structures at the Re we study are the streamwise streaks and the streamwise vortices aligned alongside them, thus L_z^+ directly restricts the streak spacing and the size of the vortices whereas L_x^+ only imposes a periodicity in the longitudinal direction. The fact that we are able to find sustained turbulence in various stages of transitions at fixed $L_x^+ = 360$, which is in the range of Newtonian–MFU streamwise sizes (Jiménez & Moin 1991), indicates that the minimal streamwise box size may not change as much as the streamwise correlation length does.

Note that there is no widely accepted definition of 'sustained turbulence'; in fact, the question of whether turbulence sustains indefinitely after the laminar–turbulence transition or eventually decays after some long but finite lifetime is still subject to controversy, especially in pipe flow where the laminar state is always linearly stable (Hof *et al.* 2006; Willis & Kerswell 2007). Here we take a pragmatic approach to this issue by checking the persistence of turbulent motion within a fixed but fairly long time interval. In all results reported in this paper, we use a statistically converged MFU solution at an adjacent parameter (typically with a slightly different Wi and/or L_z^+) as the initial condition and declare that sustained turbulence is found if the turbulent motions do not decay after 12 000 time units, which is longer than the longest natural time scale in the system (the viscous time scale, which is $O(Re)$). This is also longer than the time intervals considered in many previous viscoelastic DNS studies (Min *et al.* 2003*a*,*b*; Housiadas *et al.* 2005; Li *et al.* 2006*a*). Figure 2 summarizes our results with Newtonian runs and viscoelastic runs at $\beta = 0.97$, $b = 5000$. With the exception of one Newtonian run where we use $L_z^+ = 105.51$ (this is the size of the ECS solution when it starts to appear in an 'optimal' box; Waleffe 2003), at each Wi we test different L_z^+ with an increment of $\Delta L_z^+ = 10$, and whether sustained turbulence is found or not is recorded by filled and open symbols, respectively. Consistent with

all previous studies, L_z^+ of the MFU has an obvious dependence on Wi and increases almost monotonically with Wi. There is some roughness on the boundary between the regions where turbulence persists and where it does not; however, this phenomenon is a natural consequence of the sensitivity of turbulence in near-minimal domains to initial conditions: independent of Reynolds number, with the same parameters and box size, some initial conditions will become turbulent and some will not. Similarly, some simulation runs with box sizes larger than the 'minimal' values still laminarize, especially at high Wi. Results reported in the rest of this paper are primarily from simulation runs with the minimal L_z^+, i.e. on the boundary of filled and open symbols in figure 2. The exceptions are those with $L_z^+ < 140$, where $L_z^+ = 140$ is used instead of the actual minimal values, because it is found that at Re close to the laminar–turbulence transition, when L_z^+ is relatively small, turbulence very often tends to sustain near only one wall of the channel, while near the other wall the flow is almost laminar. One explanation is when Re is very low, the size of the minimal coherent structure is comparable to and sometimes larger than the half-channel height, so that the channel is geometrically not high enough to accommodate structures at both walls. This kind of 'single-wall turbulence' was also reported by Jiménez & Moin (1991) at Re near the laminar–turbulence transition, and is highly undesirable in our study since the flow statistics in this case are strongly biased by the laminar side. Empirically, we find that this problem does not show up for $L_z^+ \geqslant 140$, and furthermore, in all situations where we find drag reduction, the turbulence is statistically identical at both walls. So strictly speaking, we are considering the minimal flow unit for sustained turbulence at both walls. Finally, we note that intermittency between regimes of laminar and turbulent flow was never observed in our MFU simulations. In all cases, the flow either permanently laminarized or remained turbulent in the entire domain for greater than 12 000 time units.

4. Results and discussion

4.1. *Overview*

In this section, we present turbulent MFU simulation results for viscoelastic flows at various parameters. Most of the results are presented in the form of statistical averages (averages in time as well as in either the x and z dimensions or all three spatial coordinates depending on the figure). Each viscoelastic simulation run is 12 000 time units long and temporal averages are taken over the last 8000 time units. The Newtonian simulation is 20 000 time units long and the last 16 000 time units are included in the statistics.

The foremost quantity of interest with regard to drag reduction is the average streamwise velocity, as plotted in figure 3 against Wi at different β and b. Because we report simulation results at the minimum L_z^+ that sustains two-wall turbulence, the box sizes for different data points in figure 3 are in general different; the specific box size used for each data point is reported in figure 5. The corresponding degree of drag reduction is marked on the right ordinate. The error bars on the plot show the error estimates of the time-averaged quantity with the block-averaging method (Flyvbjerg & Petersen 1989). All three curves from different β and b are qualitatively similar and here we start by taking the $\beta = 0.97, b = 5000$ curve as an example. At $Wi \lesssim 16$, the pre-onset stage, U_{avg} remains at the same level as the Newtonian turbulent flow. After the onset of drag reduction at $Wi \approx 16$, $DR\,\%$ increases monotonically with Wi until $Wi \gtrsim 27$, where it starts to level off. Within the range $27 \lesssim Wi \lesssim 30$, U_{avg} is approximately independent of Wi. Recall from § 1 that MDR is identified by the

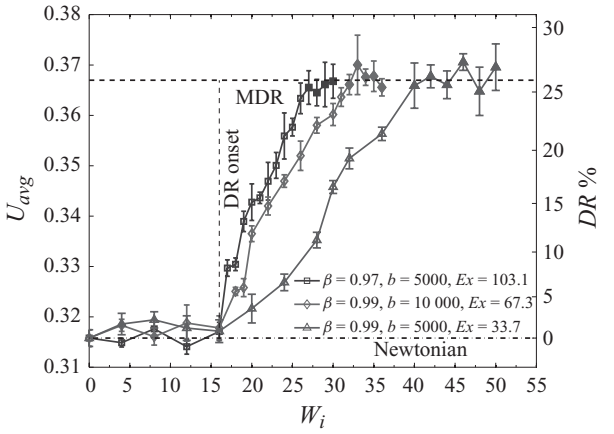

FIGURE 3. Variations of the average streamwise velocity with Wi at different β and b values (average taken in time and all three spatial dimensions); the corresponding DR % is shown on the right axis. Solid symbols represent points in the MDR stage; the horizontal dashed line is the average of all MDR points.

convergence of the friction factor (subject to the statistical fluctuations in the data), and thus U_{avg} in this plot, upon increasing Wi; this range of Wi hence corresponds to the MDR stage for $\beta = 0.97$, $b = 5000$. Simulation runs with $Wi > 30$ at these values of β and b all eventually become laminar within the 12 000 time-unit interval, regardless of the L_z^+ chosen. On the remaining two curves, $\beta = 0.99$, $b = 10\,000$ and $\beta = 0.99$, $b = 5000$, the onset of drag reduction also occurs at about $Wi_{onset} \gtrsim 16$, but the rate of increase with Wi is different. The trend of changing slope is consistent with changes in the extensibility number; higher Ex corresponds to steeper rise of U_{avg} after onset. At the high Wi end, MDR stages can be identified in both curves at $32 \lesssim Wi \lesssim 36$ and $40 \lesssim Wi \lesssim 50$, respectively, after which the flow laminarizes. There is no statistically significant difference in U_{avg} among the MDR stages for all three curves. Despite the range of parameters, all of them give $DR\,\% \approx 26\,\%$, i.e. the friction drag at MDR is constant for a given Re in spite of variations in Wi, β and b. This is, to our knowledge, the first time that this universal aspect of MDR is reproduced in numerical simulations. Figure 3 summarizes the whole data set we will present and discuss in the rest of the paper, from which we clearly see that the major components of the transitions in viscoelastic turbulent flows, including the pre-onset stage, intermediate DR and MDR are well-captured by the transient solutions in MFUs, even at Re close to the laminar–turbulence transition.

Housiadas & Beris (2003) reported full-size DNS results at $Re_\tau = 125$ ($Re = 7812.5$), $\beta = 0.9$, $b = 900$ ($Ex = 66.67$) and various Wi up to 125. With these parameters, the onset occurs at $Wi_{onset} \approx 6$, smaller than but of the same order of magnitude as our computation in MFUs. Studies on ECS solutions (Li *et al.* 2006*b*; Li & Graham 2007) predict that Wi_{onset} is around 10 and decreases slowly with increasing Re. As to the dependence of drag reduction on Wi, Housiadas & Beris (2003) found that U_{avg} increases monotonically with Wi for the whole range of Wi they studied; however, the slope drops greatly at $Wi \approx 50$. They did not see a complete convergence of U_{avg} for the range of Wi studied.

The mean velocity profiles U^+ versus y^+ of several typical points on the $\beta = 0.97$, $b = 5000$ curve in figure 3 are plotted in figure 4; for comparison, the asymptotic lines of the viscous sublayer ($U^+ = y^+$), the log-law layer of Newtonian turbulent flows

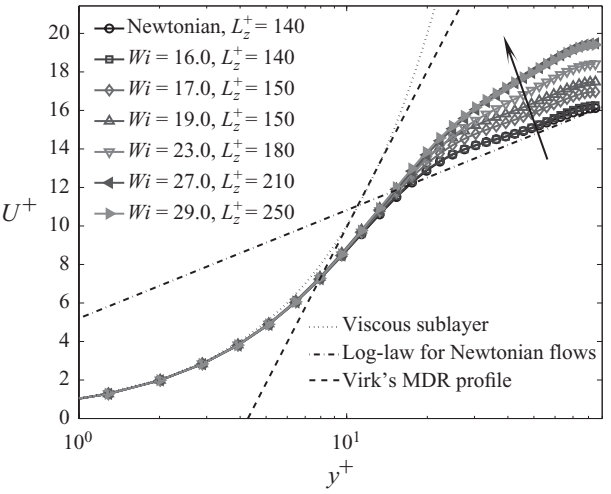

FIGURE 4. Mean velocity profiles ($\beta = 0.97$, $b = 5000$).

($U^+ = 2.44 \ln y^+ + 5.2$) (Pope 2000) and the universal profile of MDR summarized by Virk (1975) ($U^+ = 11.7 \ln y^+ - 17.0$), are also shown on the same plot. All profiles from our simulations collapse well on the viscous sublayer at $y^+ \leqslant 5$. Farther away from the wall, the Newtonian profile deviates from the $U^+ = y^+$ line in the buffer layer. Even though Re is too low in the present simulations for the log-law layer to be fully developed, the Newtonian profile still lies very close to the semi-empirical log-law at $y^+ \gtrsim 50$. Among the viscoelastic cases, except that of $Wi = 16$ which belongs to the pre-onset stage, the mean velocity profiles are all elevated compared to the Newtonian case outside the viscous sublayer. The last two curves, $Wi = 27$ and $Wi = 29$, are selected from the MDR stage and collapse well onto each other, although they are still notably lower than the Virk MDR profile. We will further discuss the mean velocity profiles in § 4.2.

In figure 2, we presented the dependence of MFU box sizes on Wi at $\beta = 0.97$, $b = 5000$; in figure 5, we show the L_z^+ values for all data points in figure 3. For the reason explained in § 3, we use a minimum of $L_z^+ = 140$ if the actual minimal box size is smaller than this value. This truncation affects at most up to $Wi \leqslant 16$ for $\beta = 0.97$, $b = 5000$ and $\beta = 0.99$, $b = 10\,000$, and $Wi \leqslant 24$ for $\beta = 0.99$, $b = 5000$, results which mostly belong to the pre-onset stage. At higher Wi, L_z^+ is larger than 140 and should faithfully reflect the size of the minimal self-sustaining coherent structures, which increases with increasing Wi with some uncertainty owing to the initial-condition dependence (§ 3). A somewhat surprising finding is that this trend persists in the MDR stage: L_z^+ changes with Wi despite the converged mean velocity profile and flow rate. This result suggests that different points within the MDR stage in figure 3 are distinguishable from one other, i.e. they are not identical solutions, but rather different dynamical structures with the same average velocity. We will further examine the similarities and differences among these solutions at the MDR stage in the later parts of this paper. Comparing results at different β and b, we observe that the values of L_z^+ in the MDR stage are close in magnitude and all fall into the range of 200–260, about twice the size of a Newtonian MFU.

Previous discussions focused on the dependence of the bulk flow rate and the length scales of MFUs on various parameters (Wi, β, b); here we examine in figure 6 the existence of possible structure–flow rate correlations by plotting L_z^+ against DR %. It

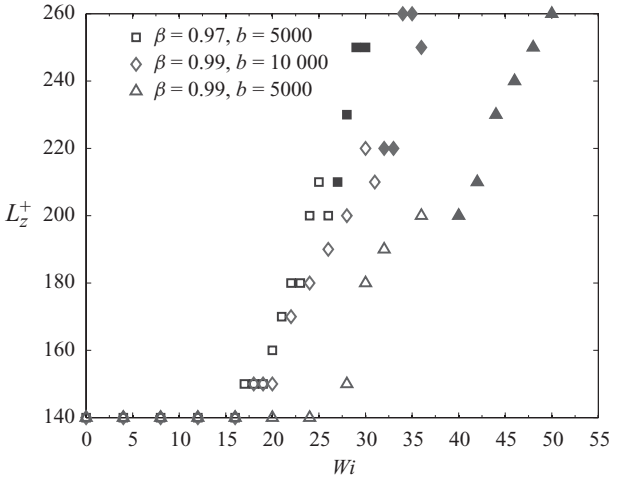

FIGURE 5. Spanwise box sizes used in this study for various parameters. Solid symbols represent points in the MDR stage.

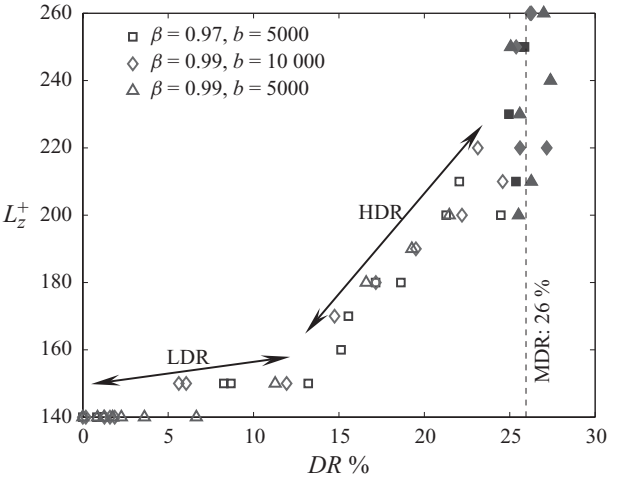

FIGURE 6. Variations of spanwise box size at different $DR\,\%$. Solid symbols represent points in the MDR stage.

is interesting to note that the dependence of L_z^+ on $DR\,\%$ is insensitive to the changes in β and b: data points from different β and b roughly fall onto a single relationship, i.e. for any given $DR\,\%$ before the MDR stage, the corresponding values of L_z^+ for different β and b are very close to one another. Note that the step size in our MFU search is $\Delta L_z^+ = 10$; the discrepancies among the $L_z^+ \sim DR\,\%$ relationships of different β or b are smaller than the methodological uncertainty. Figure 6 shows that the structural length scale increases monotonically after the onset of DR until MDR is reached at $DR\,\% \approx 26\,\%$, where L_z^+ seems to diverge: i.e. L_z^+ increases with approximately constant $DR\,\%$ and eventually turbulence does not sustain even in larger boxes.

Within the intermediate DR stage, an additional transition can be identified at $DR\,\% \approx 13\,\%$–$15\,\%$ by a sharp change in the slope of L_z^+ versus $DR\,\%$. Note

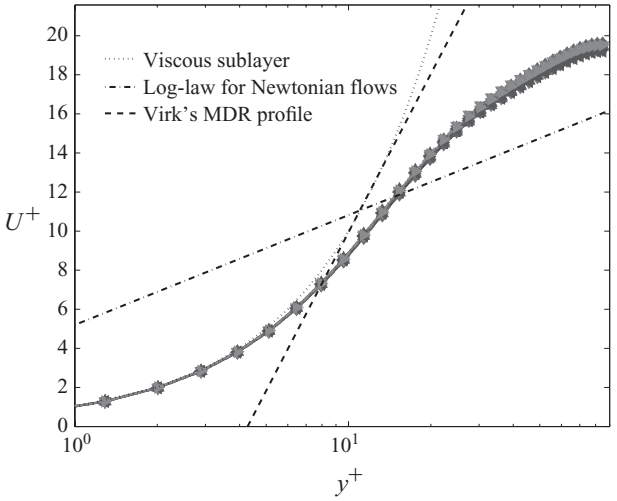

FIGURE 7. Mean velocity profiles of 15 different MDR states (Wi: 27 $\sim$ 30 for $\beta = 0.97$, $b = 5000$, Wi: 32 $\sim$ 36 for $\beta = 0.99$, $b = 10\,000$ and Wi: 40 $\sim$ 50 for $\beta = 0.99$, $b = 5000$).

that in figure 2, L_z^+ is about 140 wall units at the onset of DR, and after that L_z^+ only increases by about 10 wall units when $DR\,\%$ reaches $\sim$13 %–14 %. From $DR\,\% \approx 15\,\%$ to just before MDR ($DR\,\% \approx 25\,\%$), L_z^+ increases from $\sim$160 to $\sim$200 wall units. This transition divides the intermediate DR stage into two parts, which we will refer to as LDR and HDR below. As mentioned in § 1, the terms LDR and HDR are commonly used by other authors for $DR\,\% \lesssim 35\,\%$ and $DR\,\% \gtrsim 35\,\%$, respectively, whereas in this paper they are used to describe a qualitative transition within the intermediate stage. This transition is further discussed below.

In summary, we have found transient viscoelastic turbulence solutions in MFU at various Wi, β and b at a Re close to the laminar–turbulent transition, each of which lasts more than 12 000 units in time. By studying the parameter dependence of the bulk flow U_{avg} and the structural length scale L_z^+, the whole multistage transition sequence, including pre-onset, LDR, HDR and MDR, is observed, even though the highest $DR\,\%$ we observe is less than 30 %.

4.2. *Flow statistics*

We start our discussion of the turbulent flow statistics by revisiting the mean velocity profiles in figure 4. The six viscoelastic runs shown in that plot are selected from the pre-onset ($Wi = 16$), LDR ($Wi = 17$, $Wi = 19$), HDR ($Wi = 23$) and MDR ($Wi = 27$, $Wi = 29$) stages, respectively. The two curves at MDR overlap each other. In figure 7, mean velocity profiles of all runs in the MDR stage, including those of other Wi not shown in figure 4 and those at different β and b, are plotted together. All these profiles from different Wi, β and b collapse well onto a single curve. This profile is clearly lower than Virk's MDR profile, but is universal with respect to different polymer properties in our simulations. Within the intermediate DR stage (figure 4), there is also a difference between LDR and HDR. The two LDR profiles ($Wi = 17$ and $Wi = 19$), although shifted upward compared with the Newtonian profile, still keep roughly the same slope in the log-law layer. Most of the drag reduction occurs in the buffer layer, while the log-law layer seems unaffected and stays parallel with the Newtonian log-law, which is thus described as the 'Newtonian plug' by Virk (1975). In the HDR stage ($Wi = 23$), consistent with the experimental observations of Warholic

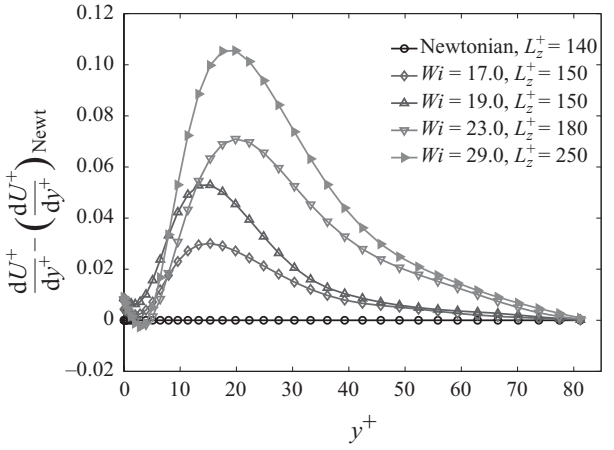

FIGURE 8. Deviations in mean velocity profile gradient from that of Newtonian turbulence ($\beta = 0.97$, $b = 5000$). LDR: $Wi = 17$, 19; HDR: $Wi = 23$; MDR: $Wi = 29$.

et al. (1999), a change in the log-law slope can also be noticed, although it is not as large as those reported at higher Re, where $DR\,\%$ is much higher. The log-law slope of the HDR profile is higher and lies between that of the Newtonian turbulence and MDR.

To see this difference more clearly, in figure 8 we plot deviations in the gradient of the mean velocity profiles from that of the Newtonian profile for several selected runs. Note that with the constant pressure drop constraint, the mean wall shear stress should be the same for all runs; in figure 8 the mean shear rate values at $y^+ = 0$ of viscoelastic solutions are slightly higher than that of the Newtonian solution because of shear thinning. Beyond the viscous sublayer, drag reduction is reflected in the increase of the gradient. For LDR ($Wi = 17$, 19), this increase is mainly localized in the buffer layer, beyond which the deviations are rather small. In HDR and MDR, the change of gradient is large and clear across the channel, except of course the viscous sublayer ($y^+ \lesssim 5$). This difference between LDR and HDR is not specific to the conditions shown in figures 4 and 8; it also exists for the other β, b pairs considered. Figure 9 illustrates this fact, showing the magnitude of $\mathrm{d}U^+/\mathrm{d}y^+$, measured at $y^+ = 40$, versus $DR\,\%$ for all MFU runs. The dependence of mean velocity profile gradient on $DR\,\%$ is roughly the same (within statistical uncertainty) at different values of β and b. A distinction in this trend can be noticed between relatively low and high $DR\,\%$: significant increase of the gradient above the buffer layer is only observed at $DR\,\% \gtrsim 14\,\%$, before which change in the gradient is small. This change coincides well with the LDR–HDR transition as identified from figure 6.

Recall that in § 4.1, we identified the stages of LDR and HDR according to the sudden change in the L_z^+ versus $DR\,\%$ relationship; here we demonstrated that this transition corresponds well to the changes in the log-law slope observed by other groups between low $DR\,\%$ and high $DR\,\%$ at higher Re (Warholic *et al.* 1999; Min *et al.* 2003*a*; Ptasinski *et al.* 2003; Li *et al.* 2006*a*). This is why we choose to use the terms 'LDR' and 'HDR', notwithstanding that our highest $DR\,\%$ is less than 30 %. The fact that this transition can be observed at $DR\,\% \approx 13\,\%$–$15\,\%$ suggests that this corresponds to a qualitative transition in the process of drag reduction instead of a quantitative effect of $DR\,\%$. Consequently, we also expect that the $DR\,\%$ of the LDR–HDR transition should be a function of Re.

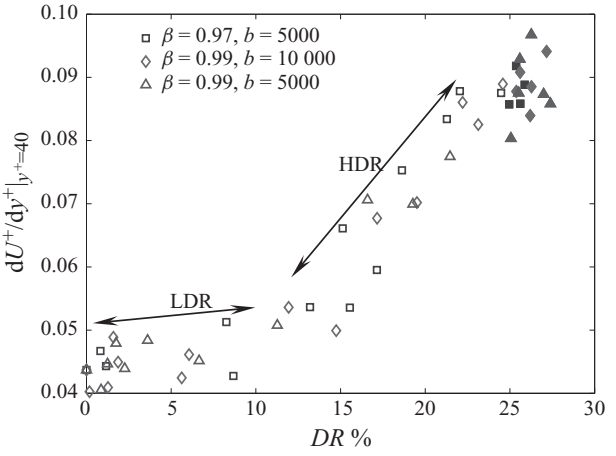

FIGURE 9. Magnitudes of mean velocity profile gradient at $y^+ = 40$. Solid symbols represent points in the MDR stage.

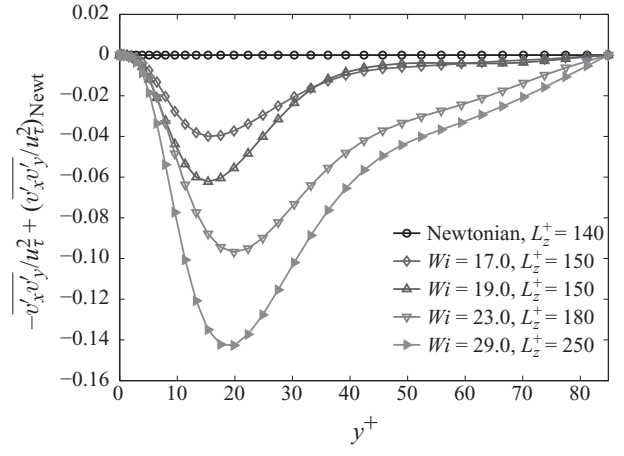

FIGURE 10. Deviations in Reynolds shear stress profiles from that of Newtonian turbulence ($\beta = 0.97$, $b = 5000$). LDR: $Wi = 17$, 19; HDR: $Wi = 23$; MDR: $Wi = 29$.

Similarly, a distinctive change also occurs in the Reynolds shear stress profiles during the LDR–HDR transition. The deviations of $-\overline{v_x' v_y'}/u_\tau^2$ with respect to the Newtonian profile are plotted in figure 10. In general, Reynolds shear stress is suppressed with increasing drag reduction. Comparing the profiles of LDR ($Wi = 17$, 19) and HDR, MDR ($Wi = 23$, 29) in figure 10, one can note that at LDR, $-\overline{v_x' v_y'}/u_\tau^2$ is suppressed mainly in the buffer layer ($5 \lesssim y^+ \lesssim 30$), and in the region $y^+ \gtrsim 40$ the deviation is barely noticeable; whereas at HDR and MDR, the deviation is substantial across the entire channel except the viscous sublayer. This distinction between local and global suppression of the Reynolds shear stress is also observed at the LDR–HDR transitions at the other values of β and b we studied. As shown in figure 11, at $y^+ = 40$ (above the buffer layer), Reynolds shear stress is substantially suppressed only after the LDR–HDR transition, which occurs at $DR\,\% \approx 13\,\% \sim 15\,\%$. The onset of HDR occurs where the dynamics of drag reduction change from being local in the buffer layer to global across the entire channel.

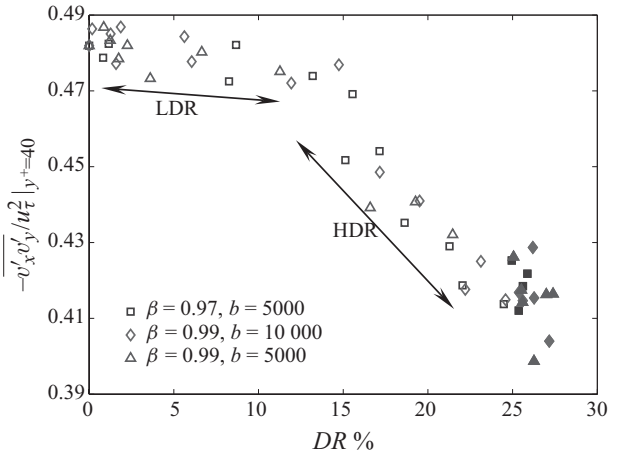

FIGURE 11. Magnitudes of Reynolds shear stress at $y^+ = 40$. Solid symbols represent points in the MDR stage.

Warholic *et al.* (1999) reported that the magnitude of Reynolds shear stress is significantly lower in HDR than in Newtonian flow, and it eventually drops to almost zero at $DR\,\% > 60\,\%$. In some other studies, however, non-zero (though still significantly smaller than Newtonian) Reynolds shear stresses were reported even for cases with more than 70 % drag reduction (Warholic *et al.* 1999; Min *et al.* 2003*a*; Ptasinski *et al.* 2003; Li *et al.* 2006*a*). Based on our study, these seemingly contradictory results can be reconciled: figure 11 shows that (above the buffer layer) although $-\overline{v_x' v_y'}/u_\tau^2$ starts to be obviously suppressed after the LDR–HDR transition, it remains at the same order of magnitude as the Newtonian value even in our MDR stage. Therefore, the quantitative magnitude of $-\overline{v_x' v_y'}/u_\tau^2$ is not the key difference between LDR and HDR; it instead might be affected by both $DR\,\%$ and Re. It is the location where $-\overline{v_x' v_y'}/u_\tau^2$ is suppressed that qualitatively indicates the transition. Indeed, despite the difference in the magnitude of Reynolds shear stress reported in those studies (Warholic *et al.* 1999; Min *et al.* 2003*a*; Ptasinski *et al.* 2003; Li *et al.* 2006*a*), one common observation is that Reynolds shear stress is substantially suppressed near the channel centre only after the LDR–HDR transition. This agreement is yet another indication that this transition, initially identified in the L_z^+ versus $DR\,\%$ plot (figure 6), corresponds to the LDR–HDR transition observed in other studies at much higher Re.

The root-mean-square (r.m.s.) velocity fluctuation profiles are shown in figures 12 and 13. After the onset of drag reduction, the streamwise velocity fluctuations (figure 12) increase with Wi until MDR is reached; meanwhile the peak of the profile moves away from the wall, reflecting the thickening of the buffer layer. Both the wall-normal (figure 12) and spanwise (figure 13) velocity fluctuations are suppressed with increasing Wi.

As to the LDR–HDR transition, the spanwise velocity fluctuation profiles show most notable differences between these two stages. In figure 13, the LDR profiles resemble that of the Newtonian turbulence in their shape, though they are lower in the magnitude. In particular, one can notice two bulges at $y^+ \approx 16$ and $y^+ \approx 46$ between which the curves are concave. This subtle concavity is absent in the HDR and MDR stages, where this part of the curve is roughly straight. Therefore, unlike turbulence in LDR where the spanwise velocity fluctuations are almost uniformly suppressed across

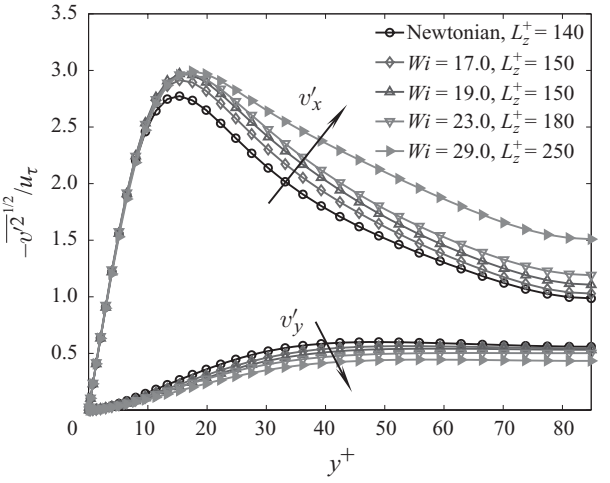

FIGURE 12. Profiles of r.m.s. streamwise and wall-normal velocity fluctuations ($\beta = 0.97$, $b = 5000$). LDR: $Wi = 17, 19$; HDR: $Wi = 23$; MDR: $Wi = 29$.

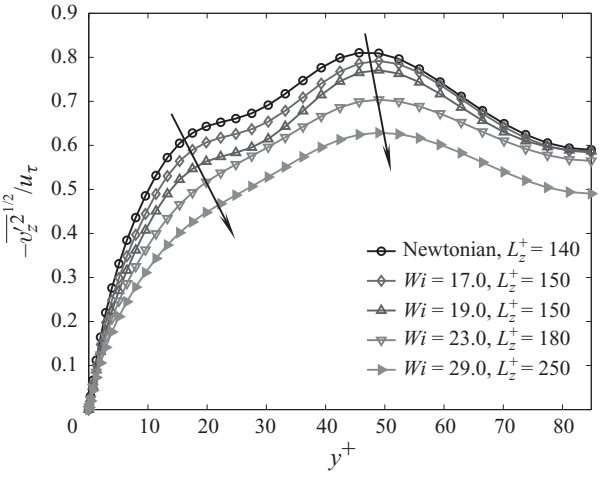

FIGURE 13. Profiles of r.m.s. spanwise velocity fluctuations ($\beta = 0.97$, $b = 5000$). LDR: $Wi = 17, 19$; HDR: $Wi = 23$; MDR: $Wi = 29$.

the channel, in the HDR and MDR stages more suppression occurs in the buffer layer and the lower edge of the log-law layer. This is also observed in the data at other values of β and b, but has not previously been reported in the literature. Meanwhile, Warholic *et al.* (1999) reported experimentally that there is a maximum in the wall-normal velocity fluctuation profiles when $DR\,\% \lesssim 35\,\%$, whereas when $DR\,\%$ is high, the maximum becomes unrecognizable. It is unclear though whether this is a quantitative effect of the substantially suppressed wall-normal velocity fluctuations, since at high $DR\,\%$ their $\overline{v_y'^2}^{1/2}/u_\tau$ profile is one order of magnitude smaller than the Newtonian profile, and the noise of the measurements can be comparable with the velocity fluctuation magnitude. In our results, there is a very subtle maximum in the Newtonian profile as well. As Wi increases, this bulge decreases in height and shrinks in size, with the lower edge moving away from the wall. At the HDR and MDR stages, the profile is almost flat after the initial rising region near the wall and the

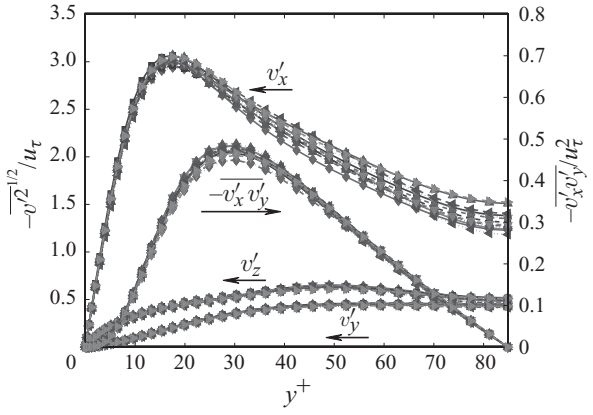

FIGURE 14. Profiles of r.m.s. velocity fluctuations and Reynolds shear stress at 15 different MDR states (Wi: 27 $\sim$ 30 for $\beta = 0.97$, $b = 5000$, Wi: 32 $\sim$ 36 for $\beta = 0.99$, $b = 10\,000$ and Wi: 40 $\sim$ 50 for $\beta = 0.99$, $b = 5000$).

bulge becomes unrecognizable. This effect, however, is not as obvious as the changes in the spanwise velocity fluctuations.

It has also been reported experimentally that notable differences between low $DR\,\%$ and high $DR\,\%$ can be observed in the streamwise velocity fluctuations (Warholic *et al.* 1999): when $DR\,\% \lesssim 35\,\%$, $\overline{v_x'^2}^{1/2}/u_\tau$ increases with $DR\,\%$ and the peak of the profile moves away from the wall; at high $DR\,\%$, $\overline{v_x'^2}^{1/2}/u_\tau$ is greatly suppressed compared with the Newtonian flows. However, as shown in figure 12, this non-monotonicity is not observed in our MFU simulations; instead, our $\overline{v_x'^2}^{1/2}/u_\tau$ profiles at different stages all follow the former (low $DR\,\%$) case in experiments. DNS studies from other groups reported contradictory results regarding whether or not this non-monotonic trend exists in streamwise velocity fluctuations (Min *et al.* 2003*a*; Ptasinski *et al.* 2003; Li *et al.* 2006*a*). The origin and significance of this discrepancy are not understood, but the fact that in those studies, comparisons between different $DR\,\%$ were made under different constraints (constant-flow rate versus constant-pressure drop) may have contributed to the complexity in this issue. Our observation (that the trend is monotonic) is consistent with Li *et al.* (2006*a*), where the constant-pressure drop constraint was also applied.

We have shown earlier that in the MDR stage, the mean velocity profiles converge to a single curve (figure 7); here we resume the discussion of the turbulence statistics in this stage. In figure 14, we plot the r.m.s. velocity fluctuations (left axis) and Reynolds shear stress (right axis) profiles for all the simulation runs in the MDR stage (corresponding to the solid data points in figure 3) with a variety of Wi, β and b. The profiles of wall-normal and spanwise velocity fluctuations converge for different parameters. The situation of the streamwise component is a bit complicated: the profiles from different parameters are very close to one another near the wall and reach maxima at very similar values in the buffer layer, while beyond the buffer layer, they spread out. To detect any possible parameter dependence of $\overline{v_x'^2}^{1/2}/u_\tau$, we have examined the distributions of its magnitudes with respect to Wi, β and b. Even though the $\overline{v_x'^2}^{1/2}/u_\tau$ profiles do not merge in the MDR stage, there is no identifiable trend of dependence of $\overline{v_x'^2}^{1/2}/u_\tau$ on any of the parameters: $\overline{v_x'^2}^{1/2}/u_\tau$ neither increases nor decreases with increasing Wi consistently in the MDR stage, and the same applies

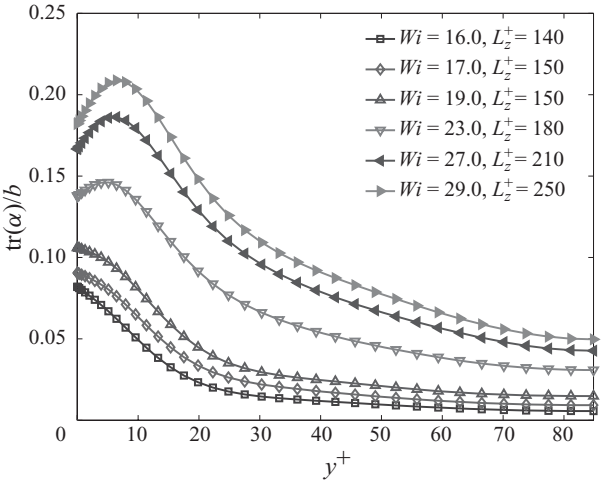

FIGURE 15. Normalized profiles of the trace of the polymer conformation tensor ($\beta = 0.97$, $b = 5000$). Pre-onset: $Wi = 16$; LDR: $Wi = 17, 19$; HDR: $Wi = 23$; MDR: $Wi = 27, 29$.

for the other two parameters (β and b). Therefore, we believe that this dispersion of $\overline{v_x'^2}^{1/2}/u_\tau$ profiles in figure 14 is a result of statistical uncertainty: it might take much longer simulation runs to obtain reliable averages on the streamwise velocity fluctuations than the other quantities we have discussed.

As to the Reynolds shear stress, the convergence is very good over most of the channel except in a small region near the maxima of the profiles at $y^+ \approx 30$; this discrepancy, as we have also examined, is again due to statistical uncertainty.

4.3. *Polymer comformation statistics*

We now turn to the statistics of the polymer conformation tensor. Figure 15 shows the mean profiles of the trace of the polymer conformation tensor $\boldsymbol{\alpha}$, which physically corresponds to the square of the end-to-end distance of the polymer chains, normalized by its upper limit b, for several selected Wi with $\beta = 0.97$ and $b = 5000$. Perhaps the most interesting observation is that although it is expected that polymers are more highly stretched as Wi increases, this trend goes on in the MDR stage. The two curves belonging to the MDR stage in figure 15 do not overlap; that is, $\mathrm{tr}(\boldsymbol{\alpha})$ keeps on increasing with Wi even though the mean velocity (as well as many other velocity statistical quantities) converges. This trend is confirmed in figure 16, where the average $\mathrm{tr}(\boldsymbol{\alpha})$ normalized by b is plotted against Wi for all simulation runs reported here. Data points in the MDR stage are filled. For every β and b, $\mathrm{tr}(\boldsymbol{\alpha})_{avg}/b$ increases monotonically with Wi: the slope is relatively low at $Wi \sim O(1)$; after the onset of drag reduction ($Wi \gtrsim 16$), the curves are steeper and $\mathrm{tr}(\boldsymbol{\alpha})_{avg}/b$ roughly rises in straight lines; $\mathrm{tr}(\boldsymbol{\alpha})_{avg}/b$ continues to increase at approximately constant slope even after MDR is reached. In addition, the ranges of $\mathrm{tr}(\boldsymbol{\alpha})_{avg}/b$ at the MDR stages of different β or b are far apart from one another even though their U_{avg} is very close; for example, at $\beta = 0.99$ and $b = 10\,000$, $\mathrm{tr}(\boldsymbol{\alpha})_{avg}/b$ is more than twice as large as that of $\beta = 0.99$ and $b = 5000$, and almost three times the magnitude at $\beta = 0.97$ and $b = 5000$. Similar to our findings, Housiadas & Beris (2003) reported in their DNS studies that while the increase of mean velocity slows down at high Wi, $\mathrm{tr}(\boldsymbol{\alpha})$ continues to increase with Wi at about the same rate.

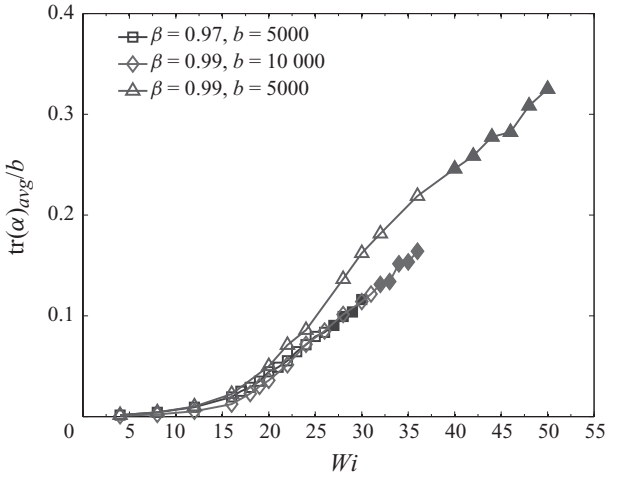

FIGURE 16. Averaged trace of the polymer conformation tensor (average taken in time and all three spatial dimensions). Solid symbols represent points in the MDR stage.

Another observation from figure 15 is that the profiles change shape with increasing Wi. At relatively low Wi, $\mathrm{tr}(\boldsymbol{\alpha})$ decreases monotonically with distance away from the wall y^+. At higher Wi, the profile becomes non-monotonic with a maximum some distance from the wall (in the buffer layer). This distance increases with increasing Wi. This observation can be explained kinematically. The process of near-wall polymer stretching is a combined effect of shear flow in the viscous sublayer and extensional flow in the buffer layer. The former is relatively more effective in stretching polymers at low Wi and the latter dominates at higher Wi; consequently, the peak location reflects the shift of the dominant kinematic effect. Although the separation between the peak location of $\mathrm{tr}(\boldsymbol{\alpha})$ and the wall in figure 15 might be thought to coincide with the LDR–HDR transition, this agreement is totally fortuitous; unlike the changes in turbulent flow statistics we studied earlier, this accordance between the Wi where the peak shifts away from the wall and the Wi at the LDR–HDR transition is specific to the choice of $\beta = 0.97$ and $b = 5000$. The lack of correlation between the peak location of $\mathrm{tr}(\boldsymbol{\alpha})$ profiles and DR % and the increasing $\mathrm{tr}(\boldsymbol{\alpha})$ in the MDR stage where the mean velocity converges suggests that the mean deformation of polymer chains is a process independent of the transitions among LDR, HDR and MDR.

Polymers exert their influence on the flow field through the polymer force term, $\boldsymbol{f}_p = 2(1-\beta)/(ReWi)(\nabla \cdot \boldsymbol{\tau}_p)$. Consequently, one might intuitively expect $\boldsymbol{f}_p$ to saturate in the MDR stage, instead of $\boldsymbol{\alpha}$ or $\boldsymbol{\tau}_p$, so that polymer would contribute equally to the momentum balance (see (2.1)) despite the differences in the magnitude of polymer stress. However, $\boldsymbol{f}_p$ profiles do not converge in the MDR stage either, although the discrepancies of $\boldsymbol{f}_p$ among different parameters are significantly smaller than those of $\mathrm{tr}(\boldsymbol{\alpha})$.

4.4. *Spatio-temporal structure*

Above we discussed statistical representations of the velocity and polymer conformation fields of MFU solutions during the multistage transitions. As these solutions contain the structural information of the essential self-sustaining process of turbulence, we turn here to the spatial and temporal nature of the flows. Figure 17 shows the spatial–temporal patterns in z and t of the shear rate $\partial v_x/\partial y$ at the lower wall $y = -1$, at fixed streamwise location $x = 0$, taken from one selected run for

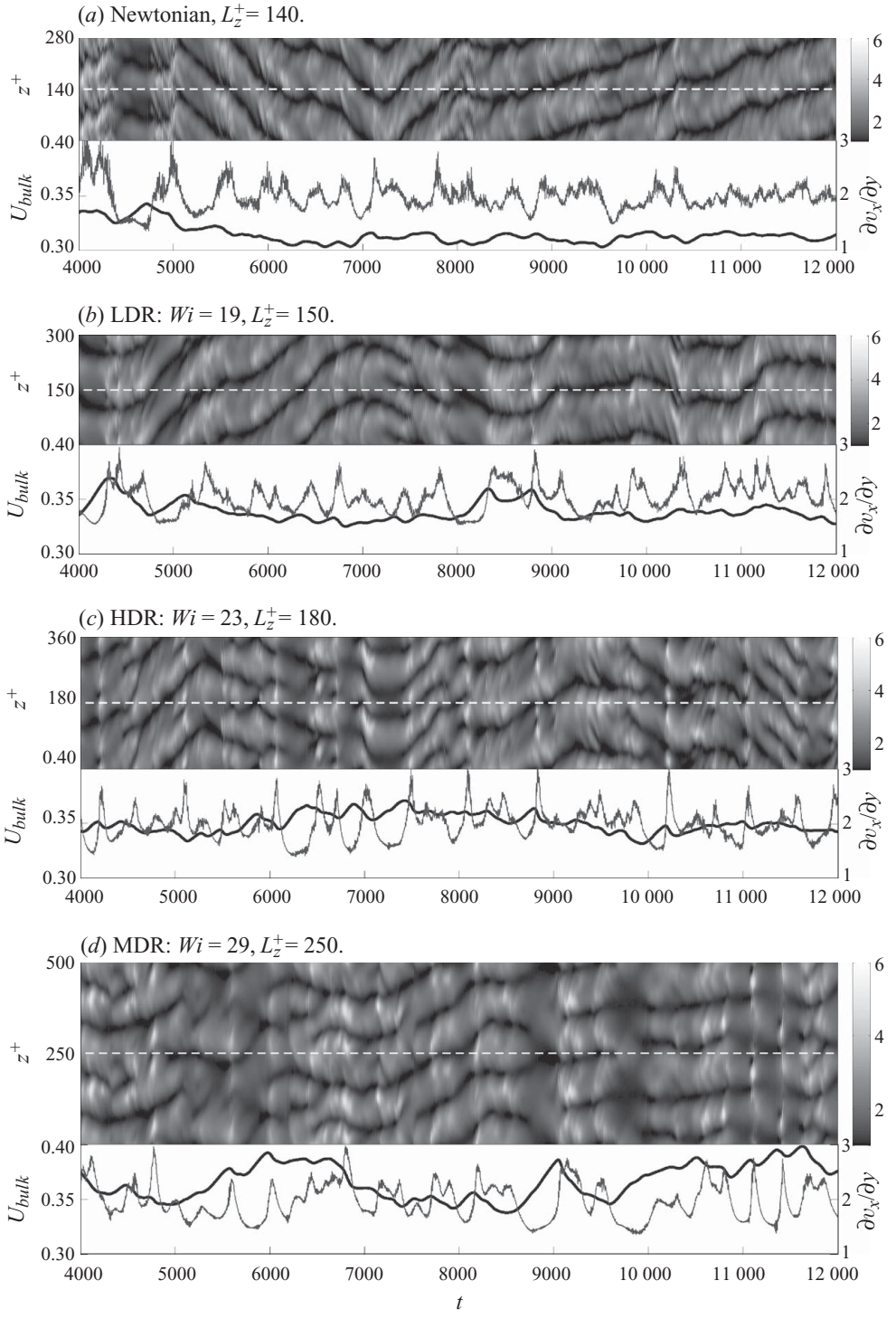

FIGURE 17. Dynamics of the self-sustaining turbulence structures at various values of Wi ($Re = 3600$, $L_x^+ = 360$, $\beta = 0.97$, $b = 5000$). Density plots show spatio temporal patterns of the wall shear rates ($\partial v_x/\partial y$ taken at $x = 0$; two periodic images are shown for each case. Note that the mean value is 2 owing to the fixed pressure gradient constraint. Line plots show (left axis and thick line) spatially averaged velocity and (right axis and thin line) average wall shear rate (average taken in the spanwise direction).

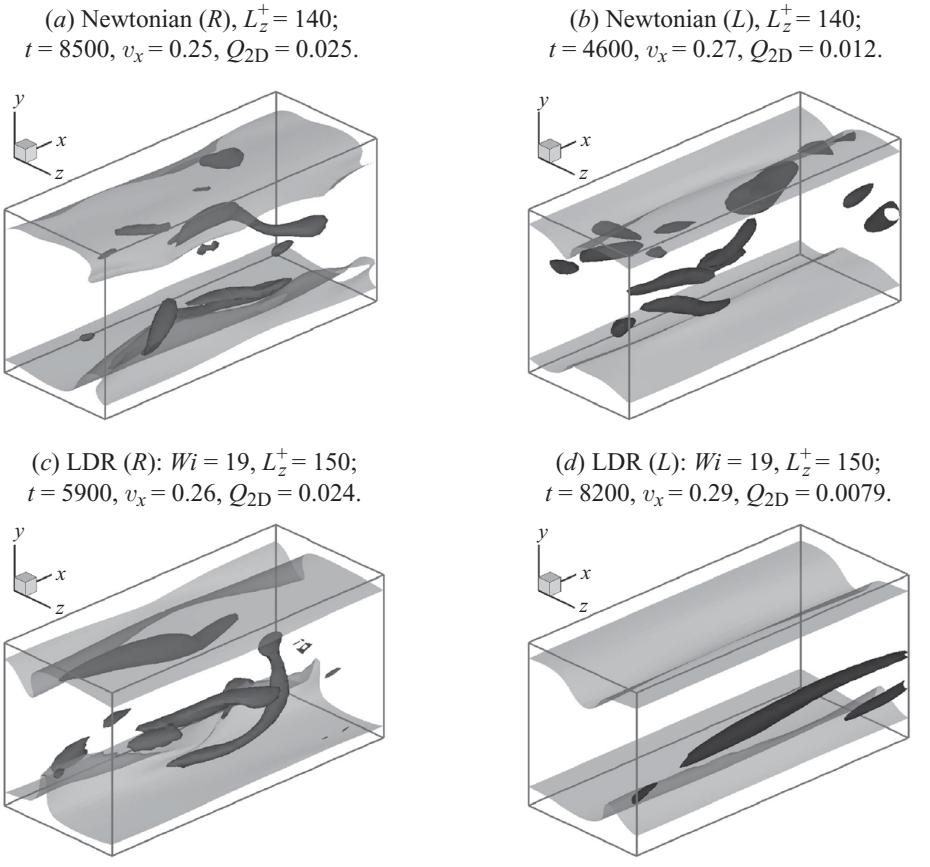

FIGURE 18. For legend see next page.

each of Newtonian turbulence, LDR, HDR and MDR. (The choice of x is arbitrary since the system is translation-invariant in x.) The distribution in the z direction of the wall shear rate is recorded every time unit and plotted in greyscale in the axes of t and z^+. A length of 8000 time units of statistically stationary turbulence is included in the plot. To aid interpretation, two periods in z are shown. Along with the wall shear rate patterns, the spatially averaged velocity U_{bulk} is also shown. Note that the time dependence of U_{bulk} is physically meaningful only in minimal flow units; in a full-scale DNS solution, the spatial average of any quantity should in principle be the same as the ensemble average and should be invariant with time. Also plotted is the z average of the wall shear rate $\partial v_x/\partial y$ as a function of time; note that the time average of this quantity is 2 owing to the fixed pressure gradient constraint.

Figure 18 shows representative snapshots of the velocity field during different stages. Two snapshots are selected for each simulation run that is shown in figure 17, marked by (*R*) and (*L*) in their captions according to the criterion to be discussed below. In each of them, isosurfaces for two quantities are plotted in a three-dimensional view of the simulation box. The flat translucent sheets with pleats are isosurfaces of streamwise velocity v_x, taken at the magnitude of $0.6v_{x,max}$, where $v_{x,max}$ is the maximum value of v_x in the domain for the given snapshot. The pleats correspond to low-speed streaks, where slowly moving fluid near the wall is lifted upward towards the centre. The dark tube-like objects are the isosurfaces of a measure of the streamwise-vortex

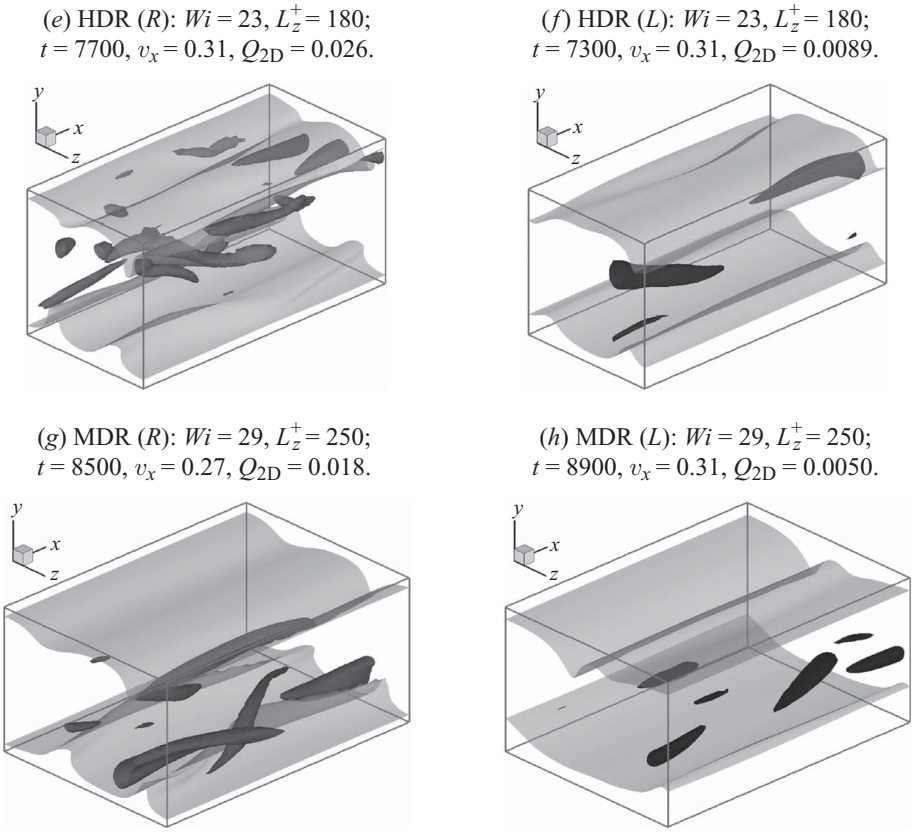

FIGURE 18. Typical snapshots of the flow field ($Re = 3600$, $L_x^+ = 360$, $\beta = 0.97$, $b = 5000$). (R) denotes snapshots chosen from 'regular' turbulence, and (L) denotes snapshots of 'low-shear' events. Translucent sheets are the isosurfaces of $v_x = 0.6v_{x,max}$; opaque tubes are the isosurfaces of $Q_{2D} = 0.3Q_{2D,max}$. The values of v_x and Q_{2D} for each plot are shown in its caption. Note that (L) states typically have much lower Q_{2D} values than (R) states. The bottom wall of each snapshot corresponds to the wall shear rate patterns shown in figure 17 at corresponding time.

strength Q_{2D}, whose definition we now describe. We apply a modified version of the Q-criterion of vortex identification (Jeong & Hussain 1995; Dubief & Delcayre 2000; Wu, Xiong & Yang 2005); that is by comparing the magnitudes of the vorticity tensor and the rate-of-strain tensor, one can identify the local regions manifesting strong vortical motions. For low Re, the buffer layer structure dominates the turbulence, so we use the Q-criterion in the y–z two-dimensional plane only to focus on vortices aligned along the mean flow direction. Specifically, we compute the two-dimensional versions of the rate-of-strain tensor $\boldsymbol{\Gamma}_{2D} \equiv (1/2)(\nabla \boldsymbol{v}_{2D} + \nabla \boldsymbol{v}_{2D}^{\mathrm{T}})$ and the vorticity tensor $\boldsymbol{\Omega}_{2D} \equiv (1/2)(\nabla \boldsymbol{v}_{2D} - \nabla \boldsymbol{v}_{2D}^{\mathrm{T}})$, where $\nabla \boldsymbol{v}_{2D} \equiv (\partial v_y/\partial y, \partial v_z/\partial y; \partial v_y/\partial z, \partial v_z/\partial z)$; then calculate the quantity $Q_{2D} \equiv (1/2)(\|\boldsymbol{\Omega}_{2D}\|^2 - \|\boldsymbol{\Gamma}_{2D}\|^2)$. Positive magnitudes of Q_{2D} would indicate regions having streamwise vortices; in figure 18, the isosurfaces of $Q_{2D} = 0.3Q_{2D,max}$ are shown, where $Q_{2D,max}$ is the maximum value of Q_{2D} in the domain for the given snapshot. Note that this varies substantially among different snapshots; the isosurface value for each image is reported in the caption.

A typical coherent structure of Newtonian turbulence contains a pair of streamwise vortices staggered alongside one sinuous low-speed streak, e.g. the structure at the

bottom wall of figure 18(*a*). The dynamics around a single streak are sufficient to make a self-sustaining process: the vortices on different sides of the streak rotate in opposite directions so that the low-speed fluid near the wall between them is lifted upward, forming the streak; instabilities of the streak will bring forth streamwise dependence into its morphology, which through nonlinear interactions further maintains the vortices (Hamilton, Kim & Waleffe 1995; Waleffe 1997; Jiménez & Pinelli 1999). In figure 17, low-speed streaks correspond to minima of the wall shear rate distributions in the z direction, which in the contour plots are observed as dark stripes. The Newtonian MFU solution (figure 17*a*) contains one almost continuous streak during the whole time range shown, which confirms that a self-sustaining process involving one streak (and the vortices around it), lasting for a very long lifetime, dominates the dynamics of the transient solution. With the translation invariance in z, the streak is not bound to any position and is free to drift in the spanwise direction. However, there are still certain periods (e.g. $6200 \lesssim t \lesssim 6800$ and $7900 \lesssim t \lesssim 8600$) when the streak appears to be quiescent and stays at the same z location for a fairly large amount of time; in some other time intervals the streak can be very active and move rapidly in the transverse direction (e.g. $5000 \lesssim t \lesssim 6200$ and $7300 \lesssim t \lesssim 7900$). The LDR stage (figure 17*b*) is qualitatively similar to the Newtonian case with one continuous streak dominating the dynamics for a long time period. In the particular case we show, there is only one break point, at $t \approx 7400$, where the first streak decays and meanwhile a second streak is growing. The minimal spanwise box size to sustain turbulence is however slightly larger, which indicates that the self-sustaining coherent structure is wider in size, resulting in an increase of streak spacing. In HDR, as shown in figure 17(*c*), the number of streaks in the minimal box varies between one and two, and complex dynamics are seen from time to time. These dynamics are also evident in MDR (figure 17*d*) where more frequently it involves two streaks although a single streak can sometimes also be found. These complex activities and dynamics of the streaks are observed through various events that change the topology of the streak patterns, including emergence of new streaks (e.g. $t \approx 11\,300$, $z^+ \approx 120$ in figure 17*c* and $t \approx 6500$, $z^+ \approx 30$ in figure 17*d*), decay of existing streaks (e.g. $t \approx 8200$, $z^+ \approx 25$ in figure 17*c*), merger of multiple (typically two) streaks into one (e.g. $t \approx 6600$, $z^+ \approx 160$ in figure 17*d*) and division of one streak into multiple streaks (e.g. $t \approx 9600$, $z^+ \approx 125$ in figure 17*d*). This transition from single-streak dynamics to multiple-streak dynamics at the LDR–HDR transition suggests that the underlying self-sustaining mechanism of turbulence may have changed; complex dynamics involving interactions between streaks might be essential in sustaining turbulent motions in HDR and MDR stages.

Recall in figure 6 that when the LDR–HDR transition occurs, the dependence of L_z^+ on $DR\,\%$ undergoes an abrupt transition; this can be interpreted based on the observations in figure 17. In the LDR stage, the underlying self-sustaining process is qualitatively the same as for the Newtonian turbulence, involving the nonlinear interactions between a single low-speed streak and the streamwise vortices on its both sides (Hamilton *et al.* 1995; Waleffe 1997; Jiménez & Pinelli 1999). Viscoelasticity reduces the drag by weakening the vortical motions (Li *et al.* 2006*b*; Li & Graham 2007) and the increase of L_z^+ is caused merely by the enlargement of the coherent structures (Li & Graham 2007). After the LDR–HDR transition, viscoelasticity is strong enough to suppress the 'Newtonian' coherent structures (as predicted by our earlier ECS study; Li, Xi & Graham 2006*b*; Li & Graham 2007), and the process involving a single isolated streak cannot sustain turbulence for a very long time (see the relatively shorter streak segments in figures 17*c* and 17*d*). As a result, a new

self-sustaining process involving inter-streak interactions arises, the details of which have yet to be elucidated. Therefore, the increase of L_z^+ in the HDR stage involves both the contribution from the enlarged structure by viscoelasticity and the extra room needed to accommodate more streaks.

As to the turbulent dynamics reflected by the evolution of U_{bulk} and the mean wall shear rate shown in figure 17, one interesting observation is that there are certain moments in the self-sustaining process when the change of U_{bulk} can be inferred by the shear rate at the wall. Specifically, during these moments, the wall shear rate is low in magnitude and its curve remains relatively smooth for $O(100)$ time units; meanwhile, the mean velocity increases steadily. Examples of these events include $t \approx 4400$ of figure 17(a), $t \approx 4200$, 4900 and 8000 of figure 17(b), $t \approx 6200$, 6900, 7300, 8800 and 10 100 of figure 17(c) and $t \approx 5500$, 5800, 8100, 8800, 9700, 11 000, 11 300 and 11 600 of figure 17(d). By comparing these temporal evolution plots with the spatial–temporal wall shear rate patterns shown in figure 17, one finds that these events usually correspond to moments when the patterns are relatively smooth; i.e. the wall shear rate has relatively small variance in both space and time. Additionally, these events appear to occur more often as $DR\,\%$ increases, although it is not easy to quantify their frequency of occurrence at this point. To a first approximation, the correlation between bulk velocity and wall shear rate can be interpreted as follows: since the driving force of the flow, the mean pressure gradient, is fixed, the change of the total momentum in the flow unit is mainly determined by the rate momentum is consumed at the wall; when shear rate at the wall is low, there is less momentum being transferred to the wall by viscous shear stress, which makes it easier to accumulate momentum in the flow unit and increase the mean velocity.

In the three-dimensional views of velocity fields shown in figure 18, one of the two snapshots presented for each run is taken from one of these 'low-shear' events, marked as (L) in the caption, and the other is from a regular turbulence interval, marked as (R). The typical snapshot of 'regular' Newtonian turbulence (figure 18a) has been discussed above. At LDR (figure 18c), the structure is qualitatively similar with one sinuous streak near each wall surrounded by streamwise vortices. At HDR (figure 18e) and MDR (figure 18g), this type of streak-vortex structure is still observed, though very often two streaks can be observed near each wall. Compared with these snapshots of 'regular' turbulence (figures 18a, 18c, 18e and 18g), those taken during the 'low-shear' events (Figures 18b, 18d, 18f and 18h) in general have much lower vortex strength, as reflected by lower Q_{2D} magnitudes. Meanwhile, the streaks are less wavy in shape: the x-dependence of the streak morphology is weak. As discussed above, these 'low-shear' events occur more frequently as $DR\,\%$ increases; therefore, we expect that in a full-scale system the probability of observing relatively straight streaks is higher in HDR and MDR stages, while at lower $DR\,\%$ the streaks should be mostly wavy. This is consistent with the observation by Li *et al.* (2006a) in full-scale DNS that long straight streaks are more predominant when the HDR regime is reached. The nature of these 'low-shear' events is as yet unclear. How these events are triggered and what roles they play in the self-sustaining processes of turbulence will be important for further understanding of drag reduction by polymers.

5. Conclusions

In this study, we consider viscoelastic turbulent flows under a variety of conditions. These flows are obtained from the minimal flow unit approach and represent the

essential coherent structures for the self-sustaining process of turbulent motions. The box size is minimized in the spanwise direction with fixed streamwise wavelength. The minimal box size to sustain turbulence increases with increasing Wi for fixed β and b, and the correlation between this length scale and the bulk flow rate is approximately universal with respect to varying β and/or b at fixed $Re = 3600$ (figure 6). At this value of Re, all key stages of transition reported previously in experiments and simulations at much higher Re are observed in the MFU solutions, including pre-onset turbulence, LDR, HDR and MDR. The discovery of the LDR–HDR transition at the current low Re and especially at a relatively low $DR\,\%$ indicates that this is a qualitative transition between two stages of viscoelastic turbulent flows and not a quantitative effect of the amount of drag reduction. Drag reduction reaches its upper limit at $DR\,\% \approx 26\,\%$ in the MDR stage, where $DR\,\%$ converges upon increasing Wi. This upper limit is universal with respect to different β and b, and it is to our knowledge the first time that the universality of MDR with respect to polymer parameters is examined in numerical simulations. After the MDR stage, which persists for a finite range of Wi at given β, b and Re, the flow returns to the laminar state.

The LDR–HDR transition is associated with a change in the underlying dynamics of the self-sustaining process of turbulence. At the LDR stage, the essential coherent structure to sustain turbulence is similar to that of Newtonian turbulence, which consists of one undulating low-speed streak and its surrounding counter-rotating streamwise vortices. At the HDR stage, the essential structure is more complicated and involves more than one streak; inter-streak interactions may be important. Nevertheless, the streamwise streaks and vortices are still the major components of the self-sustaining process in all turbulent stages in our MFU solutions. This change of the basic structure is reflected in the length scale of the MFU, resulting in a sudden change in the slope of the $L_z^+ \sim DR\,\%$ curve; the minimal box size increases more sharply with $DR\,\%$ at the HDR stage compared with the LDR stage. Several qualitative changes in flow statistics are observed during this transition, including (i) change of the log-law slope in the mean velocity profile, from the Newtonian log-law to a larger slope; (ii) disappearance of the concavity in the r.m.s. spanwise velocity fluctuation profile; and (iii) change in the location of the suppression of the Reynolds shear stress profile, from locally (in the buffer layer) at LDR to globally (in most of the channel) at HDR.

At the MDR stage, the mean velocity profiles converge onto a single curve at the given Re. The Reynolds stresses either converge to a limit or at least lose their dependence on Wi, β and b, and fluctuate within certain ranges. In contrast, the polymers are increasingly stretched by the flow with increasing Wi despite the converged flow rate, and the polymer conformation tensor continues to depend on Wi, β and b. In the MDR stage, the spatio-temporal flow structure seems similar to that of the HDR stage; the self-sustaining process also shows complex dynamics involving multiple streaks and time intervals containing relatively weak turbulent fluctuations. The minimal length scale in z to sustain turbulence keeps on increasing with Wi in the MDR stage; however, the length scale of the MFU solutions in the MDR stage under different β and b all approximately falls in the range of $200 \leqslant L_z^+ \leqslant 260$.

This study shows that the drag reduction process with varying parameters is composed of several key stages of transition, which are present in both fully developed turbulence (according to other studies) and the laminar–turbulence-transition regime. The mechanism of these transitions, especially the LDR–HDR transition and the existence of a universal MDR, is as yet unclear. Spatio-temporal images of turbulent coherent structures suggest that a shift of the underlying self-sustaining mechanism

occurs at the LDR–HDR transition. Further study of this change will be important in understanding drag reduction behaviours in HDR and MDR stages. In addition, the capability of isolating the minimal transient solutions, and the knowledge that these transitions can all be studied in the near-transition regime, will greatly facilitate future insight into the polymer drag reduction phenomenon.

This paper is dedicated to Steve Davis for his exemplary leadership in the fluid dynamics community. The authors thank Prof. F. Waleffe (Departments of Mathematics and Engineering Physics, UW-Madison) for many inspiring discussions during the course of this study. The viscoelastic DNS code used in this study is based on the Newtonian DNS code, *ChannelFlow*, authored and maintained by Dr. J. F. Gibson (Centre for Nonlinear Science, School of Physics, Georgia Institute of Technology); we are indebted to him for sharing that code and for his helpful advice on development of our code. This work is supported by the National Science Foundation (CBET-0730006).

REFERENCES

Benzi, R., De Angelis, E., L'vov, V. S., Procaccia, I. & Tiberkevich, V. 2006 Maximum drag reduction asymptotes and the cross-over to the Newtonian plug. *J. Fluid Mech.* **551**, 185–195.

Bird, R. B., Curtis, C. F., Armstrong, R. C. & Hassager, O. 1987 *Dynamics of Polymeric Liquids*, 2nd edn., vol. 2. John Wiley & Sons.

Canuto, C., Hussaini, M. Y., Quarteroni, A. & Zang, T. A. 1988 *Spectral Methods in Fluid Dynamics*. Springer.

Carlson, D. R., Widnall, S. E. & Peeters, M. F. 1982 A flow-visualization study of transition in plane Poiseuille flow. *J. Fluid Mech.* **121**, 487–505.

De Angelis, E., Casciola, C. M., L'vov, V. S., Piva, R. & Procaccia, I. 2003 Drag reduction by polymers in turbulent channel flows: energy redistribution between invariant empirical modes. *Phys. Rev.* E **67**, 056312.

De Angelis, E., Casciola, C. M. & Piva, R. 2002 DNS of wall turbulence: dilute polymers and self-sustaining mechanisms. *Comput. Fluids* **31**, 495–507.

Dimitropoulos, C. D., Sureshkumar, R. & Beris, A. N. 1998 Direct numerical simulation of viscoelastic turbulent channel flow exhibiting drag reduction: effect of the variation of rheological parameters. *J. Non-Newton. Fluid Mech.* **79**, 433–468.

Dubief, Y. & Delcayre, F. 2000 On coherent-vortex identification in turbulence. *J. Turbul.* **1**, 1–22.

Dubief, Y., Terrapon, V. E., White, C. M., Shaqfeh, E. S. G., Moin, P. & Lele, S. K. 2005 New answers on the interaction between polymers and vortices in turbulent flows. *Flow Turbul. Combust.* **74**, 311–329.

Dubief, Y., White, C. M., Terrapon, V. E., Shaqfeh, E. S. G., Moin, P. & Lele, S. K. 2004 On the coherent drag-reducing and turbulence-enhancing behaviour of polymers in wall flows. *J. Fluid Mech.* **514**, 271–280.

Faisst, H. & Eckhardt, B. 2003 Travelling waves in pipe flow. *Phys. Rev. Lett.* **91**, 224502.

Flyvbjerg, H. & Petersen, H. G. 1989 Error-estimates on averages of correlated data. *J. Chem. Phys.* **91**, 461–466.

Gibson, J. F., Halcrow, J. & Cvitanotić, P. 2008 Visualizing the geometry of state-space in plane Couette flow. *J. Fluid Mech.* **611**, 107–130.

Graham, M. D. 2004 Drag reduction in turbulent flow of polymer solutions. In *Rheology Reviews* (ed. D. M. Binding & K. Walters), pp. 143–170. British Society of Rheology.

Hamilton, J. M., Kim, J. & Waleffe, F. 1995 Regeneration mechanisms of near-wall turbulence structures. *J. Fluid Mech.* **287**, 317–348.

Hof, B., van Doorne, C. W. H., Westerweel, J., Nieuwstadt, F. T. M., Faisst, H., Eckhardt, B., Wedin, H., Kerswell, R. R. & Waleffe, F. 2004 Recurrence of travelling waves in transitional pipe flow. *Science* **305**, 1594–1597.

Hof, B., Westerweel, J., Schneider, T. M. & Eckhardt, B. 2006 Finite lifetime of turbulence in shear flows. *Nature* **443**, 59–62.

Holmes, P., Lumley, J. L. & Berkooz, G. 1996 *Turbulence, Coherent Structures, Dynamical Systems and Symmetry*. Cambridge University Press.

Housiadas, K. D. & Beris, A. N. 2003 Polymer-induced drag reduction: effects of variations in elasticity and inertia in turbulent viscoelastic channel flow. *Phys. Fluids* **15**, 2369–2384.

Housiadas, K. D., Beris, A. N. & Handler, R. A. 2005 Viscoelastic effects on higher order statistics and on coherent structures in turbulent channel flow. *Phys. Fluids* **17**, 035106.

Jeong, J. & Hussain, F. 1995 On the identification of a vortex. *J. Fluid Mech.* **285**, 69–94.

Jiménez, J., Kawahara, G., Simens, M. P., Nagata, M. & Shiba, M. 2005 Characterization of near-wall turbulence in terms of equilibrium and 'bursting' solutions. *Phys. Fluids* **17**, 015105.

Jiménez, J. & Moin, P. 1991 The minimal flow unit in near-wall turbulence. *J. Fluid Mech.* **225**, 213–240.

Jiménez, J. & Pinelli, A. 1999 The autonomous cycle of near-wall turbulence. *J. Fluid Mech.* **389**, 335–359.

Kerswell, R. R. & Tutty, O. R. 2007 Recurrence of travelling waves in transitional pipe flow. *J. Fluid Mech.* **584**, 69–102.

Kim, K., Adrian, R. J., Balachandar, S. & Sureshkumar, R. 2008 Dynamics of hairpin vortices and polymer-induced turbulent drag reduction. *Phys. Rev. Lett.* **100**, 134504.

Kim, K., Li, C.-F., Sureshkumar, R., Balachandar, S. & Adrian, R. J. 2007 Effects of polymer stresses on eddy structures in drag-reduced turbulent channel flow. *J. Fluid Mech.* **584**, 281–299.

Li, C. -F., Sureshkumar, R. & Khomami, B. 2006*a* Influence of rheological parameters on polymer-induced turbulent drag reduction. *J. Non-Newton. Fluid Mech.* **140**, 23–40.

Li, W. & Graham, M. D. 2007 Polymer-induced drag reduction in exact coherent structures of plane Poiseuille flow. *Phys. Fluids* **19**, 083101.

Li, W., Stone, P. A. & Graham, M. D. 2005 Viscoelastic nonlinear travelling waves and drag reduction in plane Poiseuille flow. In *IUTAM Symposium on Laminar–Turbulent Transition and Finite Amplitude Solutions* (ed. T. Mullin & R. R. Kerswell), pp. 289–312. Springer.

Li, W., Xi, L. & Graham, M. D. 2006*b* Nonlinear travelling waves as a framework for understanding turbulent drag reduction. *J. Fluid Mech.* **565**, 353–362.

Min, T., Choi, H. & Yoo, J. Y. 2003*a* Maximum drag reduction in a turbulent channel flow by polymer additives. *J. Fluid Mech.* **492**, 91–100.

Min, T., Yoo, J. Y., Choi, H. & Joseph, D. D. 2003*b* Drag reduction by polymer additives in a turbulent channel flow. *J. Fluid Mech.* **486**, 213–238.

Oldaker, D. K. & Tiederman, W. G. 1977 Spatial structure of viscous sublayer in drag-reducing channel flows. *Phys. Fluids* **20**, S133–S144.

Peyret, R. 2002 *Spectral Methods for Incompressible Viscous Flow*. Springer.

Pope, S. B. 2000 *Turbulent Flows*. Cambridge University Press.

Pringle, C. C. T. & Kerswell, R. R. 2007 Asymmetric, helical, and mirror-symmetric travelling waves in pipe flow. *Phys. Rev. Lett.* **99**, 074502.

Procaccia, I., L'vov, V. S. & Benzi, R. 2008 Colloquium: theory of drag reduction by polymers in wall-bounded turbulence. *Rev. Mod. Phys.* **80**, 225–247.

Ptasinski, P. K., Boersma, B. J., Nieuwstadt, F. T. M., Hulsen, M. A., van den Brule, B. H. A. A. & Hunt, J. C. R. 2003 Turbulent channel flow near maximum drag reduction: simulations, experiments and mechanisms. *J. Fluid Mech.* **490**, 251–291.

Robinson, S. K. 1991 Coherent motions in the turbulent boundary layer. *Annu. Rev. Fluid Mech.* **23**, 601–639.

Sankaran, R., Sokolov, M. & Antonia, R. A. 1988 Substructures in a turbulent spot. *J. Fluid Mech.* **197**, 389–414.

Smith, C. R. & Metzler, S. P. 1983 The characteristics of low-speed streaks in the near-wall region of a turbulent boundary-layer. *J. Fluid Mech.* **129**, 27–54.

Sreenivasan, K. R. & White, C. M. 2000 The onset of drag reduction by dilute polymer additives, and the maximum drag reduction asymptote. *J. Fluid Mech.* **409**, 149–164.

Stone, P. A. & Graham, M. D. 2003 Polymer dynamics in a model of the turbulent buffer layer. *Phys. Fluids* **15**, 1247–1256.

Stone, P. A., Roy, A., Larson, R. G., Waleffe, F. & Graham, M. D. 2004 Polymer drag reduction in exact coherent structures of plane shear flow. *Phys. Fluids* **16**, 3470–3482.

Stone, P. A., Waleffe, W. & Graham, M. D. 2002 Toward a structural understanding of turbulent drag reduction: nonlinear coherent states in viscoelastic shear flows. *Phys. Rev. Lett.* **89**, 208301.

Sureshkumar, R. & Beris, A. N. 1997 Direct numerical simulation of the turbulent channel flow of a polymer solution. *Phys. Fluids* **9**, 743–755.

Toms, B. A. 1948 Some observations on the flow of linear polymer solutions through straight tubes at large Reynolds numbers. In *Proceedings of the First International Congress on Rheology*, vol. 2, pp. 135–141. Amsterdam.

Toms, B. A. 1977 Early experiments on drag reduction by polymers. *Phys. Fluids* **20**, S3–S5.

Virk, P. S. 1975 Drag reduction fundamentals. *AIChE J.* **21**, 625–656.

Viswanath, D. 2007 Recurrent motions within plane Couette turbulence. *J. Fluid Mech.* **580**, 339–358.

Waleffe, F. 1997 On a self-sustaining process in shear flows. *Phys. Fluids* **9**, 883–900.

Waleffe, F. 1998 Three-dimensional coherent states in plane shear flows. *Phys. Rev. Lett.* **81**, 4140–4143.

Waleffe, F. 2001 Exact coherent structures in channel flow. *J. Fluid Mech.* **435**, 93–102.

Waleffe, F. 2003 Homotopy of exact coherent structures in plane shear flows. *Phys. Fluids* **15**, 1517–1534.

Warholic, M. D., Massah, H. & Hanratty, T. J. 1999 Influence of drag-reducing polymers on turbulence: effects of Reynolds number, concentration and mixing. *Exp. Fluids* **27**, 461–472.

White, C. M. & Mungal, M. G. 2008 Mechanics and prediction of turbulent drag reduction with polymer additives. *Annu. Rev. Fluid Mech.* **40**, 235–256.

White, C. M., Somandepalli, V. S. R. & Mungal, M. G. 2004 The turbulence structure of drag-reduced boundary layer flow. *Exp. Fluids* **36**, 62–69.

Willis, A. P. & Kerswell, R. R. 2007 Critical behaviour in the relaminarization of localized turbulence in pipe flow. *Phys. Rev. Lett.* **98**, 014501.

Wu, J. Z., Xiong, A. K. & Yang, Y. T. 2005 Axial stretching and vortex definition. *Phys. Fluids* **17**, 038108.

Zang, T. A. 1991 On the rotation and skew-symmetrical forms for incompressible-flow simulations. *Appl. Numer. Math.* **7**, 27–40.